Real-Space Properties of Topological and Correlated Systems

BY

SAGEN COCKLIN
B.S., University of Oklahoma, 2011

THESIS
Submitted as partial fulfillment of the requirements
for the degree of Doctor of Philosophy in Physics
in the Graduate School
of the University of Illinois at Chicago, 2020

Defense committee:

Dirk K. Morr, Chair and Advisor

Serdar Ogut

Tom Imbo

Robert Klie

Stephan Rachel, University of Melbourne

To Lafitte

Acknowledgements

I'd like to thank my advisor Dirk Morr, without whom I could not have navigated the PhD program and made it to this point. I would also like to thank my dissertation defense committee members, Prof. Tom Imbo, Prof. Robert Klie, Prof. Serdar Ogut, and Prof. Stephan Rachel. Thank you to all my friends and family who supported me in this endeavor, and a special thank you to the ones who kept me sane writing this in a global pandemic. You know who you are. Thank you.

Contribution of Authors

Chapter 1 introduces the topics covered in this dissertation. Chapter 2 is based on the published manuscript “Atomic-Scale Interface Engineering of Majorana Edge Modes in a 2D Magnet-Superconductor Hybrid System” A. Palacio-Morales, E. Mascot, S. Cocklin, H. Kim, S. Rachel, D. K. Morr, and R. Wiesendanger *Science Advances* Vol. 5, no. 7, eaav6600, 2019. A. P-M, R. W performed the experiments. E. M., S. C., S. R., D. K. M. developed and tested the theoretical model. E. M. performed the theoretical calculations discussed in the text. A. P.-M and H.K. analyzed the experimental data. D. K. M. and R. W. supervised the project. Chapter 3 is based on the published manuscript “Dimensional tuning of Majorana fermions and real space counting of the Chern number” E. Mascot, S. Cocklin, S. Rachel, and D. K. Morr, *Physical Review B* 100, 184510, 2019. Theoretical calculations discussed in the text were performed by E. M. and S. C. S. R. and D. K. M. supervised the project. Chapter 4 is based on an unpublished manuscript by S. Cocklin, M. Graham, E. Mascot, S. Rachel, and D. K. Morr. S.C. calculated the results presented in this dissertation. D. K. M. supervised the project. Chapter 5 is based on the published manuscript “Scanning tunneling shot-noise spectroscopy in Kondo systems” S. Cocklin and D. K. Morr *Physical Review B* 100, 125146, 2019. S. C. and D. K. M performed the theoretical calculations discussed in the paper and D. K. M. produced the published versions of the figures.

Contents

List of Tables

List of Figures

Summary

A thorough investigation of the real-space properties of topological superconducting system Fe/Re(0001)-O(2×1) is conducted providing strong evidence of chiral Majorana bound states (MBSs) along the edge of the system. We compare theoretical calculations of the local density-of-states (LDOS) to experimental measurements of the differential conductance, measured using scanning tunneling spectroscopy (STS) of the system and find the results to be in agreement. Further, we calculate the Chern number over a range of parameters, covering the parameters used to model the experimental results, and find that the model remains in a topological state over the parameter range, thereby providing further evidence of the topological nature of the edge states of the experimental system.

Utilizing a generic model of magnetic-superconductor hybrid materials (MSHs), we investigate the transition between one-dimensional and two-dimensional topological superconductors (TSCs). We find that by adding atoms onto 2D structures to create wires, it is possible to adiabatically transition from 2D chiral Majorana edge modes to 1D MBSs. Additionally, we find that each time we add a wire to the 2D system, we decrease the number of chiral Majorana edge modes by one, suggesting that adding wires to 2D systems is a method by which we can count the Chern number in real-space STS experiments.

Using a previously examined 5-band model of $FeSe_{0.45}Te_{0.55}$ and adding a ferromagnetic exchange term and Rashba spin-orbit coupling, we calculate the phase diagram over a wide range of global chemical potentials and exchange strengths. We find that the phase diagram hosts Chern numbers ranging from -3 to 1. We then utilize a generic model of $s_{\pm}$ topological superconductivity to investigate the appearance of MBSs at the center of a vortex core.

We consider a further extension of STS measurements where, in addition to measuring the tunneling current from the tip to the system, the zero-frequency shot noise, corresponding to the current-current correlation function, is measured. As a test bed of this measurement probe, we perform theoretical calculations of the current, shot noise, and Fano factor of a magnetic (Kondo) impurity on the surface of a simple metal. We find that, much like previously examined differential conductance measurements on such systems, there exists a characteristic asymmetry in the Fano factor. We also perform the same theoretical calculations on models of Kondo impurity lattices. As with the single impurity case, we observe a characteristic asymmetry in the Fano factor indicative of the Kondo resonance.

Chapter 1

Introduction

Starting with the discovery of the integer Quantum Hall Effect (QHE) by Von Klitzing, Dorda, and Pepper [1] in 1980 , topological materials have been been the subject of intense research efforts among condensed-matter physicists. These materials are defined by the existence of some topologically non-trivial invariant in the space of wavefunctions. In the case of QHE, Thouless, Kohmoto, Nightingale, and den Nijs showed the quantization of conductance came from an invariant that became known as the TKNN invariant in 1982 [2]. It was later shown that the TKNN invariant was equivalent to the first Chern number, an invariant well known in the mathematical theory of topology. These invariants are protected by an energy gap in the electronic states and in order to change the invariant, the gap must close. This fact can be seen in what is called the "bulk-boundary correspondance". Because the vacuum has a trivial, i.e. zero, topological invariant, but any topological material has a non-trivial, non-zero, invariant, the gap found in the bulk of the material must close at the boundary between the material and the vacuum. The result of this gap closure is the existence of in-gap electronic states that are localized at the boundary of the material. If the material is one-dimensional, these states will be zero-dimensional, if the material is two-dimensional, these states will be one-dimensional and so on.

Topological superconductors (TSCs) are topological materials whose invariant is protected by the superconducting gap. Due to the particle-hole symmetry intrinsic to superconductors, TSCs have have the potential to host exotic electronic states known as Majorana bound states (MBSs). Named after Ettore Majorana, who first theorized their existence in 1937 [3], Majorana fermions are fermions that are their own antiparticle, i.e. $\gamma^\dagger = \gamma$. In addition to being their own anti-particle, MBSs in TSCs have been theorized to exhibit non-Abelian braiding statistics [4], a feature that would allow their realization as fault-tolerant topological quantum bits [5–11].

The first model of a TSC exhibiting MBSs is known as the Kitaev chain, in which the electrons were assumed spinless and electron pairing was assumed to take place between neighboring sites, i.e. spinless p-wave superconductivity [12]. Kitaev showed that for a range of parameters, it was possible to change basis to Majorana modes, written as $\gamma_1 = c + c^\dagger$ and $\gamma_2 = \frac{c-c^\dagger}{i}$ and get two zero-energy MBSs, one at each end of the chain. However, electrons have spin and p-wave superconductivity is at present difficult to observe experimentally [13]. In order to create an experimentally feasible model, one must add spin-orbit coupling and a magnetic field. The addition of spin-orbit coupling to s-wave superconductivity results in an effective p-wave pairing correlation, while the magnetic field seperates the electrons of different spin in energy level, which mimics the spinless aspect of the Kitaev chain. In practice, this can be acheived by placing magnetic atoms on s-wave superconducting surfaces with strong spin-orbit coupling, e.g. placing iron on lead or rhenium [17,26], in order to create magnet-superconductor hybrid (MSH) systems, or by placing a semiconductor wire with strong spin-orbit coupling on the surface of a superconductor and applying a magnetic field, e.g. InSb nanowires placed on a NiTN contact [14]. This work will be concerned only with MSH systems.

Topological materials can be broken up into ten classes based on the global symmetries of their Hamiltonian [33]. The global symmetries utilized in this classification scheme are time-reversal, which materials without magnetic moments possess, particle-hole (or charge), a symmetry intrinsic to superconductivity, and chiral symmetries. By knowing how the Hamiltonian of a given model transforms under these three symmetries, along with the dimension of the material, we can determine the relevant topological invariant for the system under investigation. In this dissertation, we focus on class D topological materials, those without time-reversal symmetry or chiral symmetry, but exhibiting particle-hole symmetry. In one dimensional class D systems, the topological phases are defined by a $\mathbb{Z}_2$ invariant, while the topological phases of a two-dimensional class D material are defined by a $\mathbb{Z}$ invariant, specifically the Chern number.

Recently, a promising new route to the creation of topological superconductors has been opened in one-dimensional nano-scale hybrid systems. The reported observation of zero-energy Majorana bound states at the ends of one-dimensional (1D) Rashba-nanowire heterostructures [14–16] and of chains of magnetic adatoms on the surface of s-wave superconductors [17–20] has provided the proof of concept for the creation of these exotic quasiparticles in condensed matter systems. Similarly, it was proposed that two-dimensional (2D) topological superconductors can be created by placing islands of magnetic adatoms on the surface of s-wave superconductors [21–25]. In such systems, chiral Majorana modes – the variant of Majorana zero-energy states in 2D – are predicted to be localized near the edge of the island, and to form a dispersing, one-dimensional mode along the edge that traverses the superconducting gap. While there are strong evidence for the existence of such modes in these systems [25–27], their unambiguous identification has been experimentally hampered by the small superconducting gaps, often only of the order of a few hundred μeV. The recent report of topological superconductivity in the iron-based superconductor $FeSe_{0.45}Te_{0.55}$, as evidenced by the observation of a surface Dirac cone [28], of MBSs in the vortex core [29, 30] and at the end of a line defect [31], and of chiral Majorana mode near domain wall [32], has therefore been greeted with much enthusiasm as these systems possesses significantly larger superconducting gaps of a few meV. This work will be concerned with a theory of MBSs in vortex cores.

Theoretically predicted by Abrikosov in 1957 [34], vortices are regions in type-II superconductors where the superconducting gap reaches zero, allowing a magnetic flux quantum, $\Phi_0 = hc/2e$, to penetrate through the material. The complete suppression of the superconducting gap inside the vortex core allows for MBSs to form when vortices are present in a TSC.

FeSeTe has been shown to be well-described by a five-orbital model with 5 d-orbitals, $(d_{xy}, d_{yz}, d_{xz}, d_{x^2-y^2}, d_{3z^2-r^2})$ [80, 81]. This results in the three experimentally observed Fermi surfaces [35], two around the Γ [(0,0)] point and one around the M [($\pm\pi$,0),(0,$\pm\pi$)] and with the right choice of tight-binding parameters, can fit ARPES measurements in the vicinity of the Fermi surfaces [80]. It was argued that the surface Dirac cone of $FeSe_{0.45}Te_{0.55}$ is a consequence of the bulk being a topological insulator, and the onset of superconductivity that gaps the Dirac cone. However, the observation of a single T_c that simultaneously gaps the Dirac cone and the (so-far assumed) trivial α-, β- and γ-bands, implies a coupling between them. This coupling, however, would destroy the topological character of the Dirac cone, raising the question as to the origin of the observed MBSs. Here, we propose that the origin of the observed Majorana modes lies in the emergence of topological superconductivity in the α-, β- and γ-bands, arising from the interplay of a hard superconducting gap, a Rashba spin-orbit interaction and surface magnetism, evidence for which has been found by ARPES experiments [82]. In this case, the relevant topological invariant is the Chern number, as opposed to the $\mathbb{Z}_2$ as argued previously.

In order to probe Majorana states in TSCs, whether at the ends of nanowires, edges of

2D structures, or in vortex cores, we need local probing techniques, most notably scanning tunneling spectroscopy. An additional probe we could utilize in our study of MBSs is scanning tunneling shot noise spectroscopy (STSNS). Using this technique, in addition to examining the tunneling current, one examines the fluctuations of the tunneling current. In particular, we examine the zero-frequency shot-noise, i.e. the current-current correlation function. In order to understand what information we can extract from this new probe, we examine a well-understood correlated-electron system, namely the Kondo effect.

The Kondo effect occurs in a system with a magnetic impurity placed in a sea of conduction electrons, resulting in a quantum mechnical interaction between the localized electrons of the impurity and the delocalized conduction electrons that screen the spin of the Kondo (i.e. magnetic) impurity [36]. Its local spectroscopic signature, the Kondo resonance, has been well studied using scanning tunneling spectroscopy experiments [37–41]. By measuring the local differential conductance near magnetic adatoms such as Co located on metallic Cu(111) or Au(111) surfaces, it was observed that the Kondo resonance exhibits a lineshape (i.e., a bias dependence) with a characteristic asymmetry that can be well described phenomenologically by using the Fano formula [42]. A microscopic derivation of the Fano formula [42–44] has shown that the asymmetry of the Kondo resonance arises not only from the particle-hole asymmetry of the underlying conduction band, but also from quantum interference between electrons tunneling from the STS tip either into the conduction band, or the electronic levels of the magnetic adatoms [45].

The bulk of this dissertation focuses on the theory of MSHs. In Chapter 2, we report on a theoretical examination of the experimental system Fe/Re(0001)-O(2×1), and show strong evidence for robust topological phases in the system. This system acts as an ideal candidate system, as the interface plays a crucial role in the emergence of a topological state, allowing one to compare topological and non-topological states in one material system. We use this system to compare theoretical and experimental data and demonstrate the existence of chiral Majorana states along the edge of a MSH island. In Chapter 3, we examine the link between 1D and 2D MSHs, which are known to have different topological invariants. We demonstrate that one can adiabatically tune between the two cases, which is interesting not only because topological superconductors in 1D and 2D are in different homotopy groups – with homotopy group $\mathbb{Z}_2$ in 1D, and $\mathbb{Z}$ in 2D [46, 47] – but also because it would potentially open new possibilities to tune the nature of Majorana fermions between localized bound states and delocalized chiral edge modes.We also show that it is possible to measure the Chern number, C, using real-space properties. In Chapter 4, we calculate the phase diagram of $FeSe_{0.45}Te_{0.55}$, modeled as a symmetry class D material, and find that there exists a rich phase diagram with a variety of possible Chern numbers. Utilizing a generic model of $s_{\pm}$ superconductivity, we calculate the local density of states at the center of a vortex, in both a topological state and a trivial state and show that while both exhibit a series of Caroli-de Gennes-Matricon states, only the topological state gives a zero-energy mode, an MBS, inside the vortex. Finally, in Chapter 5, we theoretically examine the zero-frequency shot noise of single Kondo impurities on metallic surfaces as well as lattices of Kondo impurities. Given that these are theoretically and experimentally well-understood systems, these results provide insight into the use of STSNS as a novel measurement probe.

Chapter 2

Topological Superconductivity in the magnet-superconductor hybrid system Fe/Re(0001)-O(2×1)

This work was originally published as "Atomic-Scale Interface Engineering of Majorana Edge Modes in a 2D Magnet-Superconductor Hybrid System" A. Palacio-Morales, E. Mascot, S. Cocklin, H. Kim, S. Rachel, D. K. Morr, and R. Wiesendanger *Science Advances* Vol. 5, no. 7, eaav6600, 2019

In this chapter, we examine and compare theoretical and experimental evidence for the existence of topological superconductivity and chiral Majorana edge modes in the 2D magnet-superconductor hybrid system Fe/Re(0001)-O(2×1). We develop a theoretical model for the system, which we use to calculate the Chern number over a range of possible parameters, showing a rich phase diagram. For one choice of parameters, we compare the theoretical local density-of-states with the experimentally measured differential conductance and through good agreement between theory and experiment, show that the system is a topological superconductor.

2.1 Theoretical Model

To investigate the electronic structure of the Fe/Re(0001)-O(2×1) hybrid systems, we employ a Slater-Koster [66] tight-binding Hamiltonian which models the Re bulk system with the relevant surface structure as a two-dimensional system. The resulting Hamiltonian is given by:

$$H = H_{Fe} + H_{Re} + H_{FeRe} \tag{2.1}$$

$$H_{Fe} = \sum_{\langle \mathbf{r}_1, \mathbf{r}_2 \rangle} (d^\dagger_{\mathbf{r}_1} \tau_{Fe}(\mathbf{r}_1 - \mathbf{r}_2) d_{\mathbf{r}_2} + h.c.) + \sum_{\mathbf{r}} d^\dagger_{\mathbf{r}} \xi_{Fe}(\mathbf{r}) d_{\mathbf{r}} \tag{2.2}$$

$$H_{Re} = \sum_{\langle \mathbf{r}_1, \mathbf{r}_2 \rangle} (c^\dagger_{\mathbf{r}_1} \tau_{Re}(\mathbf{r}_1 - \mathbf{r}_2) c_{\mathbf{r}_2} + h.c.) + \sum_{\mathbf{r}} c^\dagger_{\mathbf{r}} \xi_{Re}(\mathbf{r}) c_{\mathbf{r}} \tag{2.3}$$

$$H_{FeRe} = \sum_{\langle \mathbf{r}_1, \mathbf{r}_2 \rangle} (d^\dagger_{\mathbf{r}_1} \tau_{FeRe}(\mathbf{r}_1 - \mathbf{r}_2) c_{\mathbf{r}_2} + h.c.) \tag{2.4}$$

where the spinors are defined via

$$c^\dagger_{\mathbf{r}} = (c^\dagger_{\mathbf{r},\uparrow}, c^\dagger_{\mathbf{r},\downarrow}, c_{\mathbf{r},\downarrow}, -c_{\mathbf{r},\uparrow}) \tag{2.5}$$

$$c^\dagger_{\mathbf{r},\sigma} = (c^\dagger_{\mathbf{r},\sigma,d_{xy}}, c^\dagger_{\mathbf{r},\sigma,d_{yz}}, c^\dagger_{\mathbf{r},\sigma,d_{zx}}, c^\dagger_{\mathbf{r},\sigma,d_{x^2-y^2}}, c^\dagger_{\mathbf{r},\sigma,d_{3r^2-z^2}}) \tag{2.6}$$

and similarly for $d^\dagger_r$. The electron creation operators $d^\dagger_r$ ($c^\dagger_r$) create an electron in the Fe 3d orbitals (Re 5d orbitals) at site $\mathbf{r}$. τ and ξ describe the hopping and on-site interaction parameters, respectively. The hopping interactions are given by:

$$\tau_{Fe}(\mathbf{r}_1 - \mathbf{r}_2) = \tau_z \sigma_0 \sum_{\beta = \{\sigma,\pi,\delta\}} V^{dd\beta}_{Fe} A^{dd\beta}(\boldsymbol{\delta}_{12}) + \alpha_{Fe} \tau_z (\boldsymbol{\sigma} \times \boldsymbol{\delta}_{12})_z L_0 \tag{2.7}$$

$$\tau_{Re}(\mathbf{r}_1 - \mathbf{r}_2) = \tau_z \sigma_0 \sum_{\beta = \{\sigma,\pi,\delta\}} V^{dd\beta}_{Re} A^{dd\beta}(\boldsymbol{\delta}_{12}) + \alpha_{Re} \tau_z (\boldsymbol{\sigma} \times \boldsymbol{\delta}_{12})_z L_0 \tag{2.8}$$

$$\tau_{FeRe}(\mathbf{r}_1 - \mathbf{r}_2) = \tau_z \sigma_0 \sum_{\beta = \{\sigma,\pi,\delta\}} V^{dd\beta}_{FeRe} A^{dd\beta}(\boldsymbol{\delta}_{12}) \tag{2.9}$$

$$\boldsymbol{\delta}_{12} = (\mathbf{r}_1 - \mathbf{r}_2)/(|\mathbf{r}_1 - \mathbf{r}_2|) \tag{2.10}$$

where τ and σ are Pauli matrices acting on particle-hole and spin degrees of freedom respectively, $A^{dd\beta}$ are the Slater Koster matrices for σ, π, and δ bonds between d orbitals, $V^{dd\beta}$ are the tight-binding hopping integrals, and α is the Rashba spin-orbit coupling. For the results below, the lattice structure of the above Hamiltonian (which determines the form of $A^{dd\beta}$) is

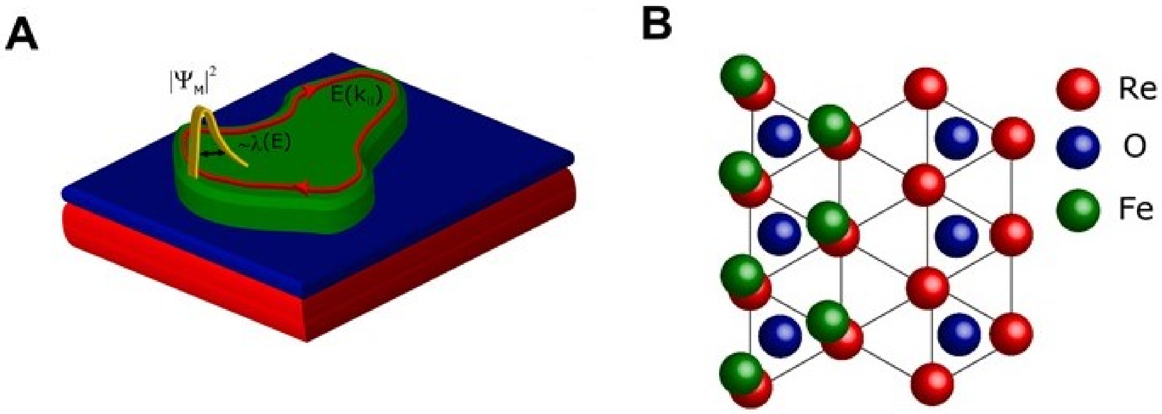

Figure 2.1: (A) Schematic picture of the Fe/Re(0001)-O(2×1) hybrid system, indicating the spatial structure of the Majorana edge modes and their spatial decay into the center of the island. Here, $k_{||}$ is the mode's momentum parallel to the edge.(B) Atomic model of the hybrid system, with the Re(0001) substrate (red spheres), p(2×1) oxide layer (blue spheres representing O atoms) and Fe adatoms (green spheres). O atoms are located above the Re hcp hollow sites and Fe adatoms are located above the Re atoms. Lattice constant of the Re(0001) surface: aRe = 0.274 nm.

shown in Fig. 2.1B. The on-site terms are given by:

$$\xi_{Fe}(\mathbf{r}) = \tau_z(\mu_{Fe}\sigma_0 L_0 + \lambda_{Fe}\mathbf{S}\cdot\mathbf{L}) + \tau_x\sigma_0\Delta_{Fe} + J\tau_0\sigma_z/2L_0 \tag{2.11}$$

$$\xi_{Re}(\mathbf{r}) = \tau_z(\mu_{Re}\sigma_0 L_0 + \lambda_{Re}\mathbf{S}\cdot\mathbf{L}) + \tau_x\sigma_0\Delta_{Re} \tag{2.12}$$

where μ is the chemical potential, λ is the spin-orbit coupling, Δ is the superconducting s-wave order parameter, and J is the magnetic exchange coupling. Explicitly, the spin-orbit term is given by:

$$\mathbf{S}\cdot\mathbf{L} = 1/2\sum_i \sigma_i L_i = 1/2\begin{pmatrix} L_z & L_x - iL_y \\ L_x + iL_y & -L_z \end{pmatrix} \tag{2.13}$$

$$L_x = \begin{pmatrix} 0 & 0 & -i & 0 & 0 \\ 0 & 0 & 0 & -i & -\sqrt{3}i \\ i & 0 & 0 & 0 & 0 \\ 0 & i & 0 & 0 & 0 \\ 0 & \sqrt{3}i & 0 & 0 & 0 \end{pmatrix} \tag{2.14}$$

$$L_y = \begin{pmatrix} 0 & i & 0 & 0 & 0 \\ -i & 0 & 0 & 0 & 0 \\ 0 & 0 & 0 & -i & \sqrt{3}i \\ 0 & 0 & i & 0 & 0 \\ 0 & 0 & -\sqrt{3}i & 0 & 0 \end{pmatrix} \tag{2.15}$$

$$L_z = \begin{pmatrix} 0 & 0 & 0 & 2i & 0 \\ 0 & 0 & i & 0 & 0 \\ 0 & -i & 0 & 0 & 0 \\ -2i & 0 & 0 & 0 & 0 \\ 0 & 0 & 0 & 0 & 0 \end{pmatrix} \tag{2.16}$$

We use a constant pairing term between orbitals of opposite L_z, i.e. $\Delta_0^{Fe(Re)} c^\dagger_{m,\uparrow} c^\dagger_{-m,\downarrow} + h.c.$ which then yields for the superconducting order parameter in the cubic harmonic basis:

$$\Delta_{Fe(Re)} = \Delta_0^{Fe(Re)} \begin{pmatrix} 1 & 0 & 0 & 0 & 0 \\ 0 & -1 & 0 & 0 & 0 \\ 0 & 0 & -1 & 0 & 0 \\ 0 & 0 & 0 & 1 & 0 \\ 0 & 0 & 0 & 0 & 1 \end{pmatrix} \tag{2.17}$$

where the sign difference between the order parameters in the Δ_{xz} and Δ_{yz} on one hand, and Δ_{xy}, $\Delta_{x^2-y^2}$ and $\Delta_{3r^2-z^2}$ is due to $Y_l^m = (-1)^m Y_l^{-m}$. We fix the superconducting order parameter of iron and rhenium, such that the energies of the coherence peaks match the experimentally measured ones, and scale down the band parameters for iron [67] to 8% and rhenium to 10%

of the original theoretical values such that the coherence length also matches the experimental values, as coherence length in the BCS theory, ξ_{BCS}, is directly proportional to the Fermi velocity, $\xi_{BCS} = \frac{\hbar v_F}{\pi \Delta}$, and hence scaling the bandwidth scales the coherence length [68]. We use the hopping integrals from rhenium scaled by 1/10 for the hopping integrals between iron and rhenium to simulate the effect of the oxide layer. The parameters are listed in Table 2.1. Note that Fe itself is not superconducting; superconductivity is only proximity-induced from the Re substrate. In order to describe the magnet-superconductor hybrid system efficiently, we consider only the effective two-dimensional system, as mentioned before. As a consequence, a superconducting order parameter for Fe, Δ_{Fe}, explicitly appears in the Hamiltonian, to account for the proximity-induced superconductivity. As the magnetic structure of the Fe island cannot be deduced from the experimental STS data obtained with a superconducting Nb-tip, we consider two magnetic structures for the Fe magnetic moments, which are typically observed on surfaces: a ferromagnetic, out-of-plane alignment [56] as well as a 120° Néel-ordered in-plane structure [57]. To directly compare the theoretically computed local density of states (LDOS) with the experimental results, we consider an Fe island with the same lattice structure and number of atoms as studied experimentally that is located on a Re(0001)-O(2×1) surface. We model the influence of the intermediate O(2×1) layer through a modification of the hybridization described by H_{FeRe}.

	Fe	Re	Fe-Re
$V^{dd\sigma}$	-3.8561 meV	-144.19 meV	-14.419 meV
$V^{dd\pi}$	2.1134 meV	66.763 meV	6.6763 meV
$V^{dd\delta}$	-0.19264 meV	-7.4015 meV	-0.74015 meV
μ	-7.04 meV	-71.5 meV	
λ	2.4 meV	32 meV	
Δ_0	0.528 meV	0.33 meV	
J	17.473 meV		
α	2.4 meV		

Table 2.1: Tight binding parameters for the Fe/Re(0001)-O(2×1) hybrid system.

Additionally, in order to demonstrate the universality of the combined spatial and energy evolution of Majorana edge modes shown below, we consider a previously introduced generic model for a topological superconductor described by the Hamiltonian [21, 23]

$$H = \sum_{\mathbf{r},\mathbf{r}',\sigma} \left(-t - \mu\delta_{\mathbf{r},\mathbf{r}'}\right) c^{\dagger}_{\mathbf{r}\sigma} c_{\mathbf{r}'\sigma} + \Delta \sum_{r} c^{\dagger}_{\mathbf{r}\uparrow} c^{\dagger}_{\mathbf{r}\downarrow} + i\alpha \sum_{\mathbf{r},\alpha\beta} c^{\dagger}_{\mathbf{r},\alpha} \left(\hat{\boldsymbol{\delta}} \times \boldsymbol{\sigma}\right)^{z}_{\alpha\beta} c_{\mathbf{r}+\hat{\boldsymbol{\delta}},\beta}$$

$$+ J \sum_{\mathbf{R},\alpha,\beta} \mathbf{S}_{\mathbf{R}} \cdot c^{\dagger}_{\mathbf{R}\alpha} \boldsymbol{\sigma}_{\alpha\beta} c_{\mathbf{R}\beta} + \text{H.c.} \tag{2.18}$$

where $c^{\dagger}_{\mathbf{r},\alpha}$ creates an electron at lattice site $\mathbf{r}$ with spin α, and σ is the vector of spin Pauli matrices. Moreover, α denotes the Rashba spin-orbit coupling arising from the breaking of the inversion symmetry at the surface [17] with $\boldsymbol{\delta}$ being the vector connecting nearest neighbor sites. Due to the full superconducting gap, which suppresses Kondo screening, we consider the magnetic moments to be static in nature, such that $\mathbf{S}_{\mathbf{R}}$ is a classical vector representing the direction of the adatom's spin located at $\mathbf{R}$, and J is its exchange coupling with the conduction electron spin.

2.2 Calculation of Local Density of States

The orbital and spin resolved LDOS at site $\mathbf{r}$, orbital α, spin σ, and energy E is obtained from the retarded Green's function via

$$\rho(\mathbf{r}, \alpha, \sigma, E) = -\frac{1}{\pi} Im G_{ret}(\mathbf{r}, \alpha, \sigma, \mathbf{r}, \alpha, \sigma, E) \tag{2.19}$$

where the retarded Green's function is given by

$$G_{ret}(\mathbf{r}, \alpha, \sigma, \mathbf{r'}, \alpha', \sigma', E) = \langle \mathbf{r}, \alpha, \sigma | (E + i\delta - H)^{-1} | \mathbf{r'}, \alpha', \sigma' \rangle \tag{2.20}$$

$$= \sum_{k} \frac{(\langle \mathbf{r}, \alpha, \sigma | k \rangle \langle k | \mathbf{r'}, \alpha', \sigma' \rangle)}{(E + i\delta - E_k)} \tag{2.21}$$

and k and E_k are the eigenvectors and eigenvalues of the Hamiltonian matrix H. The local density of states at site $\mathbf{r}$ and energy E are the sum of the orbital and spin resolved LDOS at site $\mathbf{r}$ and energy E.

$$\rho(\mathbf{r}, E) = \sum_{\alpha,\sigma} \rho(\mathbf{r}, \alpha, \sigma, E) \tag{2.22}$$

Only states with $E_k \approx E$ contribute to the sum in equation 2.21, and we therefore calculated 100 eigenvectors for each E using the Lanczos algorithm. The spatial LDOS was calculated for each site and smoothed using a Gaussian kernel convolution to simulate the STM tip interacting with nearby sites calculated as $\rho_{smooth} = \int_{sites} \frac{d\mathbf{r}'}{\sigma\sqrt{2\pi}} e^{\frac{-(\mathbf{r}-\mathbf{r}')^2}{2\sigma}}$. To match the spatial resolution of the experiment, the spatial LDOS was pixelated where the pixel width, w_p, is the spatial resolution and the LDOS for sites inside a pixel were summed. We used $w_p = 1$ nm, and $w_p = 0.33$ nm for Figs. 3.3 and 3.5, respectively, and $w_p = 0.7$ nm for Fig. 2.6.

2.3 Calculation of the Chern number

Let $P(\mathbf{k})$ denote the projector onto occupied states in crystal momentum space

$$P(\mathbf{k}) = \sum_{E_n(\mathbf{k})<0} |\Psi_n(\mathbf{k})\rangle\langle\Psi_n(\mathbf{k})| \tag{2.23}$$

where $n(\mathbf{k})$ is the band index at crystal wave vector $\mathbf{k}$ and $\Theta(-E_{n(\mathbf{k})})$ is the Heaviside function at energy $-E_{n(\mathbf{k})}$. The Chern number is given by the formula:

$$C = \frac{1}{2\pi i} \int_{BZ} Tr(P(\mathbf{k})[\partial_{k_x} P(\mathbf{k}), \partial_{k_y} P(\mathbf{k})]) dk_x dk_y \tag{2.24}$$

where Tr denotes the trace, square brackets denote the commutator, and the integral runs over the full Brillouin zone. The phase diagram in Fig. 3.4C was generated by computing P($\mathbf{k}$) at points in the neighborhood of $\mathbf{k}$ to approximate the partial derivatives using the central difference method [69], then integrated using an adaptive quadrature rule [70]. The parameter V_{FeRe}/V_{Re} used in Fig. 3.4C is the ratio of hybrid coupling to rhenium coupling which is kept the same for each bond, i.e. $V^{dd\alpha}_{FeRe}/V^{dd\alpha}_{Re} = V_{FeRe}/V_{Re}$ for $\alpha \in \{\sigma, \pi, \delta\}$.

2.4 Results

To demonstrate the creation of topological superconductivity and the ensuing chiral Majorana modes through interface engineering in 2D magnet-superconductor hybrid structure, the Wiesendanger group have grown nano-scale Fe islands of monoatomic height on the (2×1) oxygen-reconstructed (0001) surface of the s-wave superconductor Re under ultra-high vacuum (UHV) conditions. The insertion of an atomically thin oxide separation layer between magnetic Fe island and the superconducting Re surface is shown to be crucial for the emergence of a topologically non-trivial superconducting state, which is absent when the Fe island is deposited directly on the surface of the superconducting Re substrate. The spatially- and

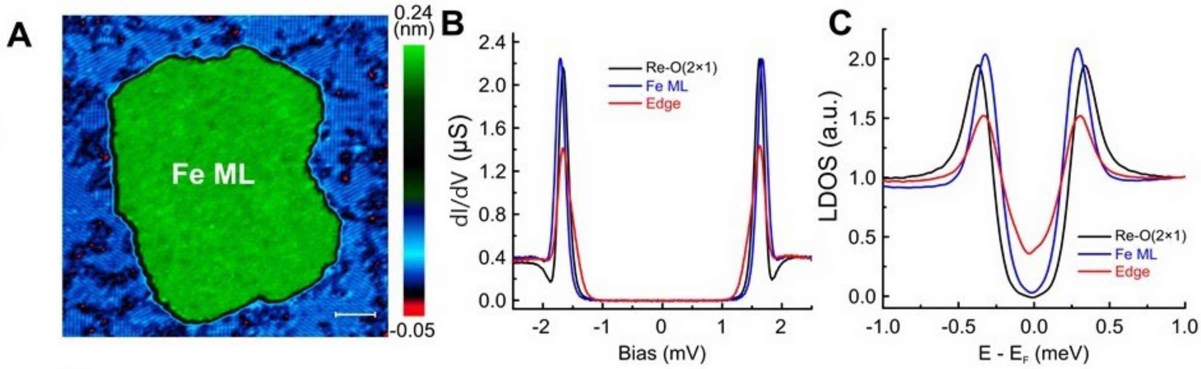

Figure 2.2: (A) Constant-current STM image of a small Fe island located on the O(2×1) surface (scale bar: 5 nm). (B) Experimentally measured dI/dV spectrum on the O(2×1) surface (black line), in the center (blue line) and at the edge (red line) of the Fe island. As all STS measurements were performed with a superconducting Nb tip whose gap size is $\Delta_{tip}^{Nb} = 1.41meV$, the coherence peaks are located at $\Delta_{tip}^{Nb} + \Delta_{O(2\times1)}$ or $\Delta_{tip}^{Nb} + \Delta_{Fe}$, respectively. This yields a measured superconducting gap of $\Delta_{O(2\times1)} \approx 280\mu eV$ in the O(2×1) layer, and of $\Delta_{Fe} \approx 240\mu eV$ in the center of the Fe island. (C) Deconvoluted dI/dV spectrum on the O(2×1) surface (black line), in the center (blue line) and at the edge (red line) of the Fe island. Parameters for constant-current STM images and stabilization conditions for STS measurements: U= 2.5 mV, I= 1.0 nA, T= 360 mK.

energy-resolved differential tunneling conductance, dI/dV, was measured in situ using a low-temperature scanning tunneling microscope (STM) with a superconducting Nb tip to improve the energy resolution.

A constant-current STM image of the Fe/Re(0001)-O(2×1) hybrid system with a single nano-scale Fe island is shown in Fig. 2.2A. In general, it is not possible to identify the relative positions of the Fe- and O-atoms with respect to the Re surface atoms from STM images. However, DFT studies [49] suggest that the O-atoms are located above the hcp hollow sites of the Re(0001) surface, forming a p(2×1)structure, as confirmed by topographic surface profiles from the STM image.

Moreover, our theoretical analysis discussed below suggests that the Fe atoms are located directly above the surface Re atoms, thereby continuing the ABAB stacking of the Re bulk lattice with the intermediate O atoms located above the Re hcp hollow sites. The resulting atomic structure of the hybrid system is displayed in Fig. 2.1B. The raw dI/dV measured above the O(2×1) surface with a superconducting tip is shown in Fig. 2.2B. To account for the energy dependence of the density of states in the tip, the Wiesendanger group deconvolute the raw dI/dV using standard methods (see SI sec. S3 of ref. [26]), yielding the deconvoluted dI/dV shown in Fig. 2.2C. The energies of the coherence peaks reveal a superconducting gap of $\Delta_{O(2\times1)} \approx 280\mu eV$ which is slightly lower than that measured on the pure Re(0001) surface

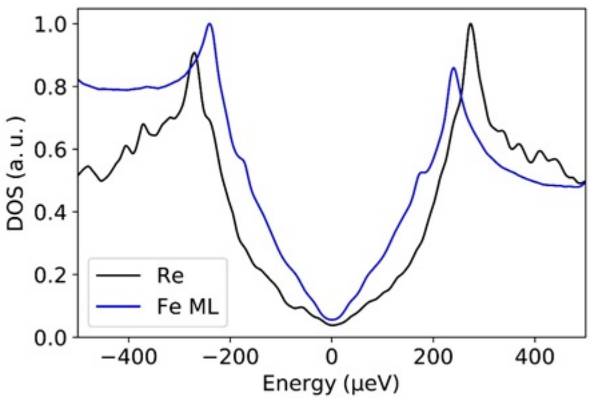

Figure 2.3: Theoretically computed LDOS. Theoretically computed LDOS on the Re(0001)-O(2×1) surface (black line) and on the Fe ML (blue line). The position of the coherence peaks is shifted from $\Delta_{O(2\times1)} \approx 280\mu eV$ on the Re(0001)-O(2×1) surface to $\Delta_{Fe} \approx 240\mu eV$ on the Fe ML. The finite LDOS at zero energy arises from the finite electronic damping, Γ, introduced for computational reasons in the calculations.

($\Delta_{Re} \approx 330\mu eV$). Spectroscopic measurements on different structural domains of the O(2×1) layer indicate a uniform spatial distribution of the superconducting gap.

A necessary requirement for the emergence of topological superconductivity is that the Fe islands couple magnetically to the superconducting Re surface. The observation in dI/dV of a Yu-Shiba-Rusinov (YSR) in-gap state [50–54] near an isolated magnetic Fe adatom located on top of the O(2×1) surface demonstrates the existence of the magnetic coupling to the superconducting Re surface, despite the presence of an intermediate oxide layer. Moreover, the presence of the nanoscale Fe island gives rise to the formation of a band of YSR states near the O(2×1) gap edge [23]. As a result, dI/dV measured in the middle of the Fe island reveals a smaller superconducting gap $\Delta_{Fe} \approx 240\mu eV$ than that of the O(2×1) layer (see Fig. 2.2C). In Fig. 2.3, we present the resulting theoretical LDOS on the Re(0001)-O(2×1) surface, and on the Fe ML, which reproduce the experimentally measured positions of the coherence peaks.

A hallmark of 2D topological superconductors is the existence of dispersive, in-gap Majorana modes that are spatially located along the edges of the system [23, 55] (Fig. 2.1A). To visualize the existence of such modes, we present in Figs. 3.3A-F (Figs. 3.3G-L) the raw (deconvoluted) spatially resolved differential tunneling conductance, in and around the nano-scale Fe island shown in Fig. 2.2A, with increasing energy, from E_F up to the energy of the coherence peak at Δ_{Fe}. At E_F (Fig. 3.3G), the dI/dV map exhibits a large intensity along the edge of the Fe island (confined to within a distance of 5 nm from the edge), clearly indicating the existence of an in-gap edge mode expected for a topological superconductor. With increasing energy

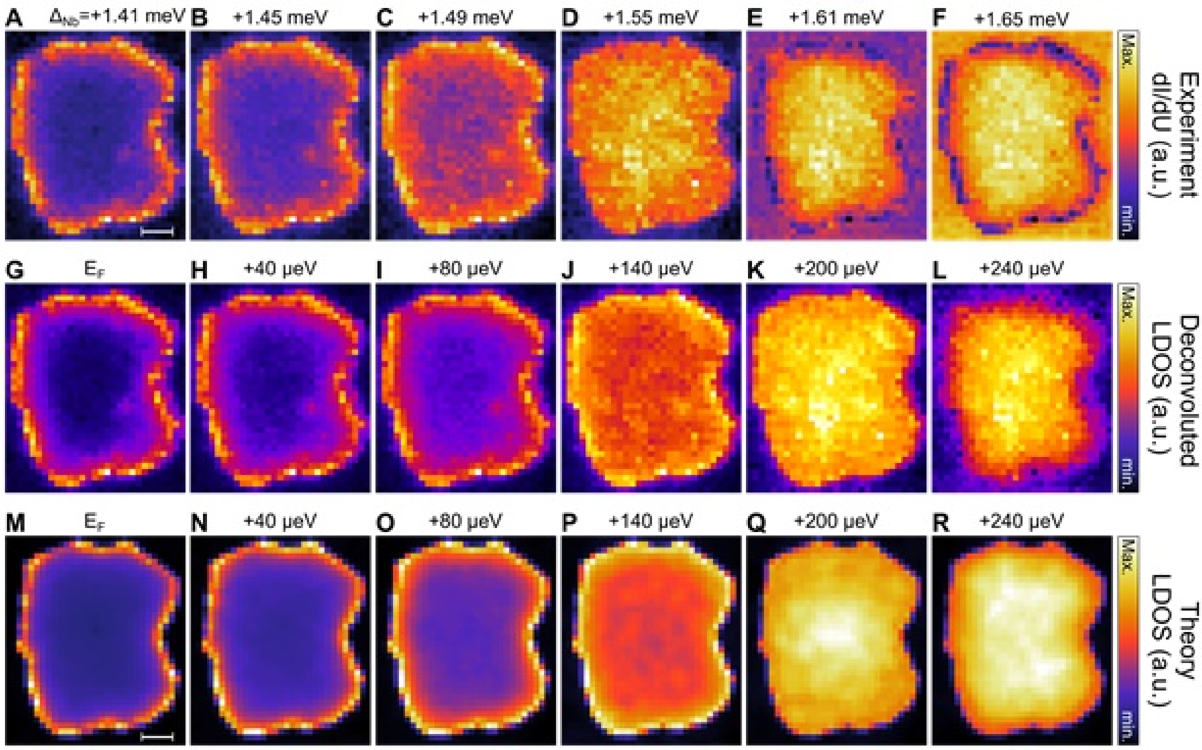

Figure 2.4: Evolution of the edge states for the hybrid system Fe/Re(0001)-O(2×1) with increasing energy. (A-F) Experimentally measured differential tunneling conductance maps and corresponding deconvoluted data sets (G-L) for the Fe island shown in Fig. 2.2A from the Fermi level $E_F = \Delta_{tip}^{Nb}$ to $\Delta_{Fe} = 240\mu eV$ above E_F. At low energies (A-C and G-I), the dI/dV map reveals states that are localized along the edges of the Fe island (edge modes). Once the localization length of the edge modes becomes of the size of the island (D and J), the dI/dV in the center of the island is comparable to that along the edges. (M-R) Theoretically computed spatially resolved local density of states for the same energies as in G-L. The theoretical data have been spatially convoluted to reproduce the experimental resolution. STS measurement conditions: U= 2.5 mV, I= 1.0 nA, T= 360 mK. The intensity scale is adjusted for each figure separately. Scale bars in A and, M: 5 nm.

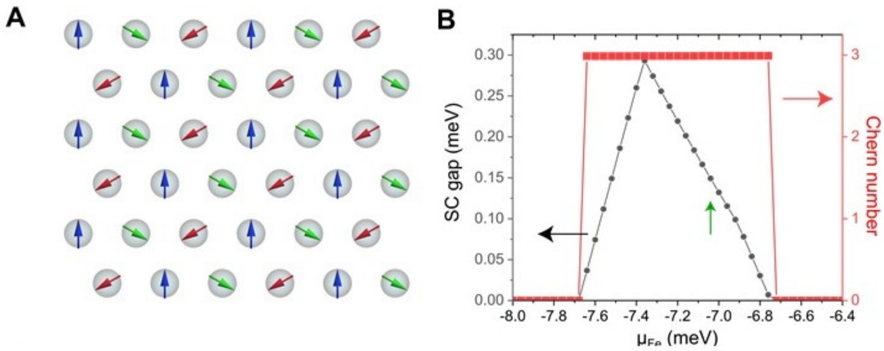

Figure 2.5: Topological phase diagram. (A) 120° Néel-ordered in-plane configuration of the Fe moments. (B) Superconducting gap (black) and Chern number (red) for a range of μ_{Fe}. The Chern number is 3 when the system is gapped and 0 when the gap closes. The hybrid couplings V_{FeRe} are set to zero and $\alpha_{Fe} = 1.6meV$, $\lambda_{Fe} = 0.48meV$, and $\Delta_{Fe} = 2.24meV$. As expected, the Chern number changes when the gap closes.

(Fig. 3.3H and, I) the edge mode begins to extend further into the island, consistent with an increase in the mode's localization length, λ(E) (Fig. 2.1A) (see discussion below). Note that the dI/dV measured inside the Fe island and along the edge are of similar intensity already for energies below Δ_{Fe}, when the localization length becomes comparable to the size of the Fe island (Fig. 2J, $E \approx \pm 140\mu eV$, see discussion below). Increasing the energy even further reverses the intensity pattern, such that at the energy of the coherence peaks $\Delta_{Fe} \approx \pm 240\mu eV$ (Fig. 3.3L) the dI/dV intensity at the edge is smaller than that in the island's center.

For a ferromagnetic structure, the theoretically computed spatial and energy dependence of the LDOS (Figs. 3.3M-R) agrees well with that of the deconvoluted experimental differential tunneling conductance (Figs. 3.3G-L). Similarly, the theoretically computed LDOS inside the Fe island and of the bare Re(0001)-O(2×1) surface also shows a reduction of the superconducting gap in the former (see Section 5.1), in agreement with the experimental findings (Fig. 2.2C). Moreover, computing the topological invariant [58] for the parameters used in Figs. 3.3M-R, we obtain a Chern number C=20. These results taken together strongly suggest that the edge modes shown in Fig. 3.3 are chiral Majorana modes arising from an underlying topological superconducting state in the Fe/Re(0001)-O(2×1) hybrid system. Note that uncertainties in the band parameters, and in particular in the hybridization strength, might affect the actual value of the Chern number, but will not result in a topologically trivial phase (see discussion below). Similarly, we find that the system is a topological superconductor for a 120° Néel-ordered in-plane structure [57] [Fig. 2.5A] of the Fe moments with Chern number C=3 [Fig. 2.5B].

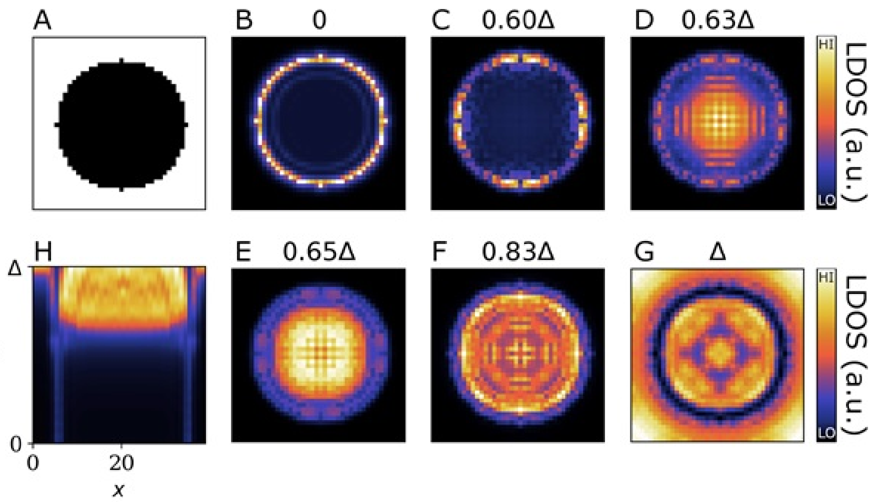

Figure 2.6: Energy evolution of the spatially resolved LDOS for a generic topological superconductor. (A) Schematic picture of a ferromagnetic Shiba island with large black circles denoting magnetic defect sites. (B-G) Spatially resolved LDOS from E_F to Δ for $\mu = -4t$, $\alpha = 0.8t$, $\Delta = 1.2t$, and $J = 2t$. Such a large value of Δ is necessary in order to obtain a coherence length that is smaller than the size of the island, otherwise no well- defined edge modes can be observed. As the energy increases, the weight of the LDOS moves from the edge of the magnetic island toward the center, similar to the results shown in Fig.3.3. (H) Intensity plot of the LDOS as a function of position (along a cut through the island) and energy, showing the energy evolution of the edge modes.

In order to show that the observed behavior of the LDOS is not particular to the system observed and modeled here, we examine the corresponding behavior of our generic model. We consider a two-dimensional square lattice, with a circular magnetic island of radius $15a_0$, as shown in Fig. 2.6A. In Fig. 2.6B-G, we present the energy evolution of the LDOS, which is qualitatively similar to that shown in Fig. 3.3 for the Fe/Re(0001)-O(2×1) hybrid structure. Moreover, a plot of the LDOS as a function of position (along a cut through the island) and energy shown in Fig. 2.6H reveals that the chiral Majorana mode is located at the edge of the island for all energies up to the superconducting gap edge. We therefore conclude that the combined spatial and energy evolution of the topological Majorana edge modes, as reflected in the LDOS, is universal, and does not depend on a particular band structure.

A further important signature of Majorana modes is that they are topologically protected against edge disorder according to the bulk-boundary correspondence [55]. Indeed, edge modes that possess a trivial, non-topological origin can easily be moved away from the Fermi energy, or even be destroyed by disorder. However, the experimentally studied Fe island does not only possess a spatial symmetry different from the underlying Re(0001)-O(2×1) surface, but also exhibits a large degree of disorder along its edges (Fig. 2.2A). The fact that despite this

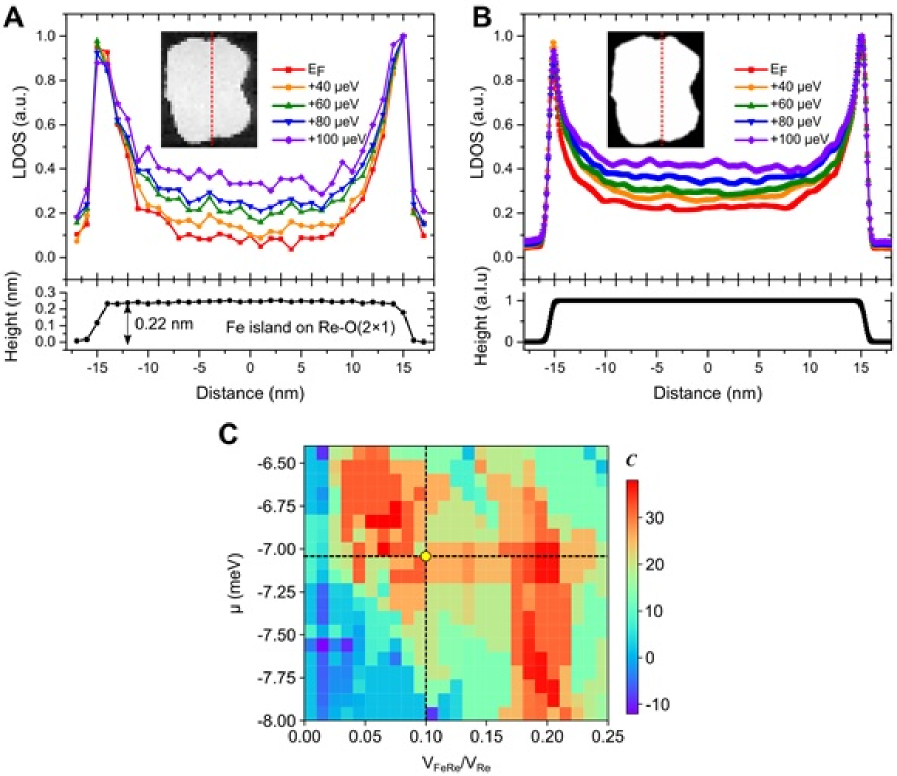

Figure 2.7: Decay of the edge states inside an Fe island. (A) Deconvoluted LDOS profiles obtained from the experimentally measured dI/dV spectra along the red dotted line in the inset for several different energies: E_F, +40 μeV, +60 μeV, +80 μeV, and +100 μeV. (B) Theoretically computed LDOS along the red line in the inset for the same energies as in A. The corresponding surface profiles of the island are depicted in the lower panels of A and B. The theoretical results have been spatially convoluted to reproduce the experimental resolution. Inset in A and B: the STM topography image and theoretically considered model structure of an Fe island, respectively. All LDOS profiles in A and B are normalized by their maximum values at the island's edge. (C) Theoretical phase diagram of the hybrid system. Chern number for an out-of-plane ferromagnetic structure of the Fe layer, as a function of V_{FeRe}/V_{Re} and μ_{Fe}. The phase diagram reveals an abundance of topological phases near the parameter set used to describe the Fe/Re(0001)-O(2×1) hybrid system (yellow dot with crossed dotted lines).

disorder, edge modes are observed at E_F, further supports our conclusion that these modes are topologically protected chiral Majorana modes.

To further elucidate the properties of the Majorana edge modes, we present in Fig. 3.4 the deconvoluted differential tunneling conductance (Fig. 3.4A) and the theoretically calculated LDOS (Fig. 3.4B) for increasing energy along a cut through the Fe island, as shown in the insets (the surface profile of the island is shown in the lower panels of Fig. 3.4A and B). Both quantities agree quantitatively and decay as expected exponentially into the island with a localization length λ(E) that increases with increasing energy (as sketched in Fig. 2.1A). The maxima in dI/dV and the LDOS are located right at the edge of the island for all energies, as expected from generic models of topological superconductors with a dominant s-wave order parameter [25] (see discussion below). This very good agreement between the topographically determined edge of the Fe island and the maximum in dI/dV therefore provides additional evidence for the topological nature of the edge modes. Note that the recently reported spatial splitting of the edge mode [25] can only be understood if one assumes a topological superconductor with a predominant p-wave order parameter [25], or if the edge mode starts to hybridize with bulk states [24].

The question naturally arises to what extent the observed topological superconducting phase of the Fe/Re(0001)-O(2×1) hybrid system is robust against variations in the strength of parameters, such as the hybridization between the Re surface and the Fe island, V_{FeRe}, which is mediated by the O(2×1) oxide layer, or the chemical potentials, μ_{Fe} or μ_{Re}. To investigate this question, we present in Fig. 3.4C the topological phase diagram of the system, as a function of V_{FeRe} and μ_{Fe} (the Chern number was calculated as described in Section 2.3, and the parameters for the system considered above are indicated by a yellow circle). The phase diagram clearly reveals an abundance of topological superconducting phases in close proximity to each other that are characterized by different Chern numbers. While the uncertainty in the electronic band parameters we have used to describe the Fe/Re(0001)-O(2×1) system can result in an uncertainty of the actual Chern number in the experimentally realized system, the fact that the system resides in a topological phase is robust. This substantiates our conclusion that the observed edge modes directly reflect the topological nature of the magnet-superconductor hybrid system.

To demonstrate that interface engineering using an atomically thin oxide layer is crucial for the emergence of topological superconductivity in the Fe/Re(0001)-O(2×1) hybrid system, we contrast the above results with those obtained when the Fe layer is directly deposited on the Re(0001) surface without an intermediate oxide layer [57] (see Fig. 3.5). In this case, with the Fe atoms being located directly above the Re(0001) hcp hollow sites (Fig. 3.5H), dI/dV measured on the Fe islands exhibits no signature of edge modes in the raw data (Fig. 3.5E-G) as well as in the deconvoluted data (Fig. 3.5I-K); rather it reflects delocalized, bulk-like excitations throughout the entire Fe island at E_F. Our theoretical analysis of this system reveals (using the same set of parameters as for Fig. 3.3M-R) that the change in the spatial location of the Fe atoms with respect to the Re(0001) surface (arising from the missing intermediate oxide layer) renders the electronic structure of this hybrid system gapless. As a result, the LDOS at E_F is non-zero, leading to the delocalized excitations observed experimentally. Moreover, the absence

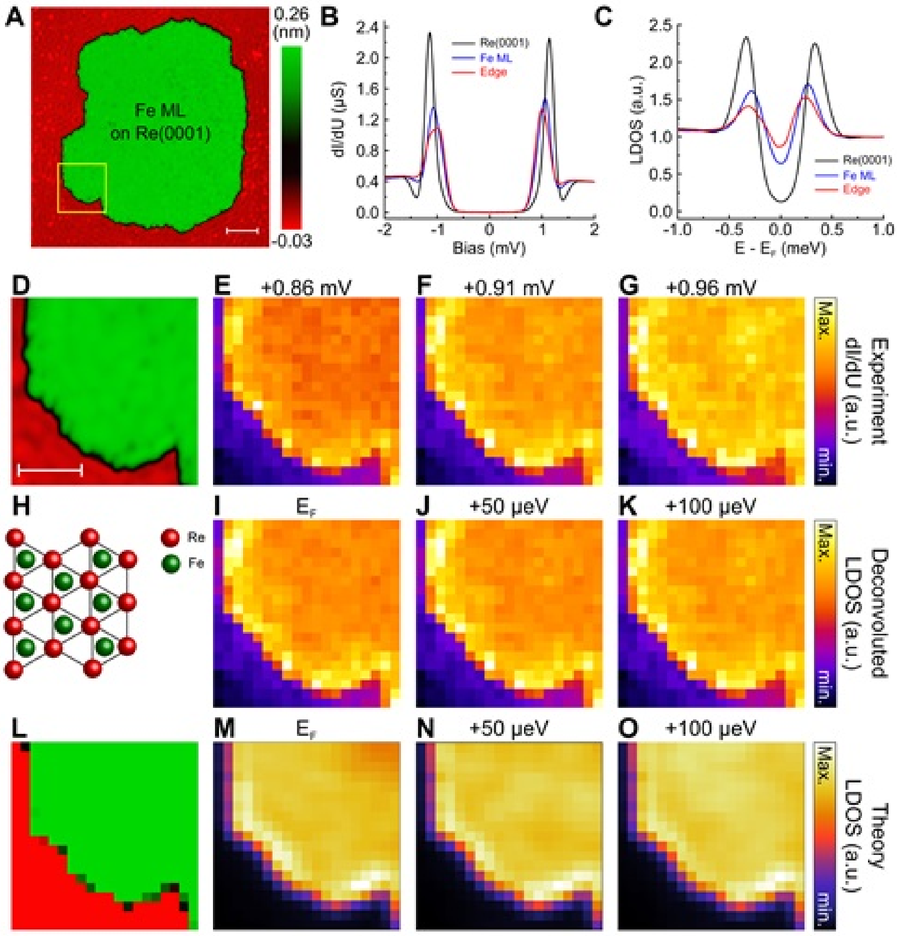

Figure 2.8: Topological trivial Fe island on a bare Re(0001) surface. (A) The STM image of the Fe island being placed directly on the superconducting Re substrate (scale bar: 10 nm). (B) Experimentally measured dI/dV spectra on the clean Re(0001) surface (black), at the center (blue) and at the edge (red) of the Fe island using a superconducting Nb-tip whose gap size is $\Delta_{tip}^{Nb} = 0.86meV$. (Tunneling conditions for STM/STS measurements: U = 2.0 mV, I = 1.0 nA, T= 360 mK). (C) The deconvoluted surface LDOS derived from the spectra shown in B taking into account the superconducting gap of the Nb tip used for the STS measurements. (D) A zoomed-in STM image of the Fe island shown in A (yellow boxed area in A); (scale bar: 5 nm). (E-G) Experimentally measured dI/dV maps for the Fe island shown in D at U=+0.86, +0.91 and +0.96 mV, which are corresponding to the energy of E_F, 50 and 100 μeV, respectively. (H) Atomic model of the Fe island on the bare Re(0001) substrate. Fe adatoms are located at the hollow sites of the Re substrate. (I-K) The spatial distribution of the deconvoluted surface LDOS for the island shown in D. (L) The zoomed-in image of the theoretically considered Fe island structure, reproducing the experimental Fe island in D. (M-O) Calculated LDOS of the island shown in L at the same energies as the experimental results. The theoretical data have been spatially convoluted to reproduce the experimental resolution.

of a gap implies that the system is in a trivial, non-topological phase, explaining the absence of edge modes, as observed experimentally. Thus the change in the relative position of the Fe and Re atoms induced by the presence of the oxide layer is crucial for realizing topological superconductivity in the hybrid system.

Chapter 3

Dimensional Tuning of Majorana Fermions and the Real Space Counting of the Chern Number

This work was originally published as "Dimensional tuning of Majorana fermions and real space counting of the Chern number" E. Mascot, S. Cocklin, S. Rachel, and D. K. Morr, *Physical Review B* 100, 184510, 2019

In this chapter, we explore the transition between one- and two- dimensional topological superconductors. We demonstrate that it is possible to use atomic manipulation techniques to adiabatically tune between one-dimensional and two-dimensional topological superconductors in magnet-superconductor hybrid (MSH) structures. By adding Shiba wires to Shiba islands and observing the spatial distribution of the local density-of-states, we show that we can count the Chern number using real-space measurements. Additionally, we extend these results from a toy model to the experiementally relevant model used in the previous chapter for Fe/Re(0001)-O(2×1).

3.1 Model

To investigate the engineering of Majorana fermions, we consider MSH structures in which magnetic adatoms are placed on the surface of a conventional s-wave superconductor with a Rashba spin-orbit interaction. Realizations of such MSH structures include Fe on Pb(110) [17, 19, 20] as well as Fe on Re(0001) [18] or Re(0001)-O(2×1) [26]. While the Fe-Pb systems form a rectangular lattice the Fe-Re systems form a hexagonal lattice. Such systems are described by the Hamiltonian previously introduced in Ch. 2, eqn. 2.18. For concreteness and linkage with the above mentioned experiments, we consider both square and triangular lattices. We emphasize that all results remain true for other lattice geometries as expected for topologically non-trivial matter.

While the topological phases of macroscopic, translationally-invariant systems are well characterized by the topological invariant – the Chern number, see eqn. 2.24, the topological phases of inhomogeneous [77] or finite-size systems can be characterized by the spatial Chern number density given by

$$C(\mathbf{r}) = \frac{N^2}{2\pi i}\mathrm{Tr}_{\tau,\sigma}[P[\delta_x P, \delta_y P]]_{\mathbf{r},\mathbf{r}} \ . \tag{3.1}$$

with the Chern number in real space then give by [69, 76] $C = 1/N^2 \sum_{\mathbf{r}} C(\mathbf{r})$. Here, $\mathrm{Tr}_{\tau,\sigma}$ denotes the partial trace over spin σ and Nambu space τ,

$$\delta_i P = \sum_{m=-Q}^{Q} c_m e^{-2\pi i m \hat{x}_i/N} P e^{2\pi i m \hat{x}_i/N} \ , \tag{3.2}$$

and the projector P onto the occupied bands is given by $P = \sum_{\alpha=\mathrm{occ.}} |\psi_\alpha\rangle \langle\psi_\alpha|$ for a real-space $N \times N$ lattice. The c_m's are central finite difference coefficients for approximating the partial derivatives. The coefficients for positive m can be calculated by solving the following linear set of equations for $c = (c_1, \ldots, c_Q)$: $\hat{A}c = b, A_{ij} = 2j^{2i-1}, b_i = \delta_{i,1}, i, j \in \{1, ..., Q\}$. For negative m, we have $c_{-m} = -c_m$. We have taken the largest possible value of $Q = N/2$. $C(r)$ as defined above thus represents the real-space analog of the Berry curvature $\mathcal{F}(k)$, and was previously introduced to discuss the topological phases of Chern insulators [78].

3.2 Dimensional tuning and counting of Majorana modes

The observation of zero-dimensional (0D) Majorana modes at the ends of Shiba chains, and chiral 1D majorana modes at the edges of Shiba islands have raised the question of whether atomic manipulation techniques can be used to tune Majorana modes between these two limits. To address this question, we consider a system in which both the 1D chains and 2D islands of magnetic adatoms induce topological superconductivity, with Chern number $C = -1$ in the latter case. To interpolate between Shiba chains and islands, we attach an increasingly longer chain of magnetic adatoms to a Shiba island, as shown in Figs. 3.1(a)-(c). With no chain present,

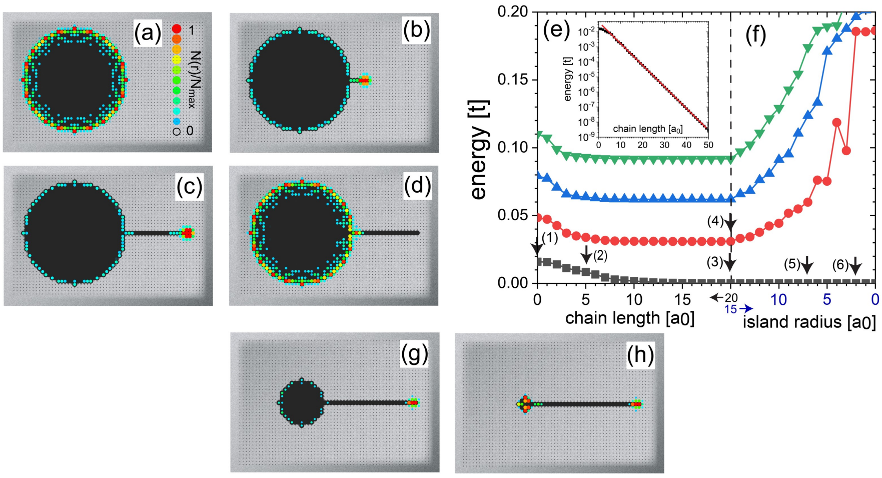

Figure 3.1: MSH hybrid structure consisting of a Shiba island of radius $R = 15a_0$ (with $C = -1$) and chain with parameters $(\mu, \Delta, \alpha, J) = (-4t, 1.2t, 0.45t, 2.6t)$ (black circles denote sites with magnetic adatoms.). (a)-(c) LDOS of the lowest energy Majorana mode with increasing chain length, corresponding to arrows (1)-(3) in (e). (d) LDOS of the second lowest energy Majorana mode, corresponding to arrow (4) in (e). (e) Evolution of the 4 lowest energy levels with increasing chain length, in units of the island radius, $R_0 = 15a_0$, of the Shiba island. Inset: log-plot of the lowest energy level with increasing chain length, red line represents a linear fit. (f) Evolution of the 4 lowest energy levels with decreasing island radius, in units of R_0. (g),(h) LDOS of the lowest energy Majorana mode with decreasing radius, corresponding to arrows (5),(6) in (f).

the Shiba island possesses a chiral Majorana mode that is localized near the edge of the island, and forms a dispersing, 1D edge mode that traverses the superconducting gap. Each chiral edge mode is comprised of two Majorana fermions, which for the lowest energy mode are located at small, but finite energy $E = \pm\epsilon$ [Fig. 3.1(e)] (this non-zero energy, and the discreteness of the modes arises from the finite size of the island [23]). The LDOS of the lowest energy mode is shown in Fig. 3.1(a). When a chain is attached to the island, and its length is increased, spectral weight is transferred from the island's lowest energy Majorana edge mode to the end of the chain [Fig. 3.1(b)]. When the chain is sufficiently long [Fig. 3.1(c)] it possesses a localized Majorana fermion at its end, while a second Majorana fermion remains delocalized along the edge of the island. Note that the spatially integrated spectral weight of the zero-energy state is exactly split between the dispersive Majorana edge fermion and the bound state at the end of the chain. Concomitant with the increasing separation between these two Majorana fermions, the energy of the lowest energy states decreases smoothly and monotonically [Fig. 3.1(e)], implying that the system remains in a topological phase throughout this evolution, i.e., without undergoing a phase transition. Moreover, as expected for two Majorana fermions localized at the end of a chain, the log-plot of their energy shown in the inset of Fig. 3.1(e) reveals that it decreases exponentially with the length of the chain. At the same time, the higher energy Majorana modes remain entirely localized along the edge of the island, as shown in Fig. 3.1(d) for the second lowest energy state. We note that as there is no zero-energy crossing of the lowest energy states with increasing chain length, no parity transitions occurs [74]. To finally arrive at a purely one-dimensional chain, we next reduce the radius of the Shiba island, while keep the length of the chain fixed. In Fig. 3.1(f), we present the evolution of the four lowest energy states with decreasing island radius. As expected, we find that the lowest energy state, corresponding to the Majorana fermions located at the end of the chain and around the edge of the island, remains located near zero energy with decreasing R, while the other states move up in energy. The corresponding lowest energy LDOS are shown in Figs.3.1(g),(h), demonstrating that the Majorana fermions remain located at the end of the chain with decreasing R. The smooth evolution of the lowest energy states shown in Fig. 3.1(f) demonstrates that the system can be adiabatically tuned, i.e., without undergoing a phase transition, between the island-chain structure shown in Fig. 3.1(c), and a purely 1D chain shown in Fig. 3.1(h). This implies that the entire transition from the 2D Shiba island in Fig. 3.1(a) [corresponding to the left hand side in Fig. 3.1(f)] to the 1D chain [corresponding to the right hand side of Fig. 3.1(g)] is adiabatic, and the system does not undergo a phase transition.

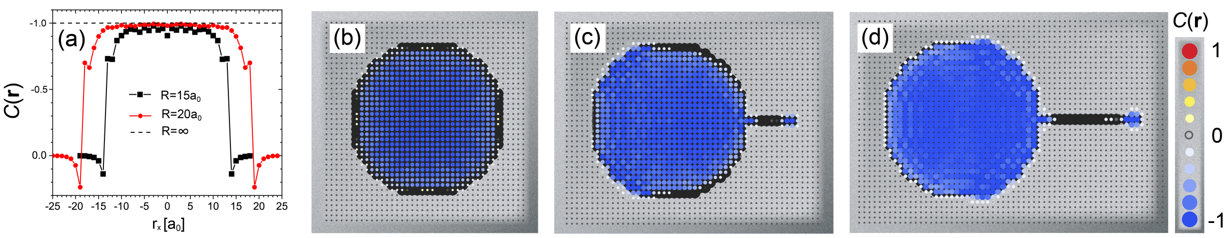

Figure 3.2: (a) Linecut of the Chern density $C(\mathbf{r})$ through a Shiba islands of different radii R. Spatial plot of $C(\mathbf{r})$ for the MSH structures in Fig. 3.1 with chain length (b) $L = 0$, (c) $L = 10$ and (d) $L = 20$. Parameters are the same as in Fig. 3.1 with $C = -1$.

Further evidence for the adiabatic evolution of the system come from considering the Chern number density, $C(\mathbf{r})$ of the MSH structure. $C(\mathbf{r})$ can be employed to characterize the topological nature of finite-size (or disordered [77]) systems, as it adiabatically connects the topological state of finite size systems to the Chern number of translationally invariant, macroscopic systems. To demonstrate this, we compare in Fig. 3.2(a) the Chern number density along a line cut through Shiba islands with increasing radius, with $C(\mathbf{r})$ of an infinitely large system. Already for an island with radius $R = 15a_0$, $C(\mathbf{r})$ in the center of the island is close to that of the infinitely large system, an agreement which improves with increasing island radius. At the same time, the island exhibits chiral edge modes, thus demonstrating that the Chern number density is a suitable property to characterize the topological nature of a finite-size Shiba island.

Thus, we can now employ $C(\mathbf{r})$ to further demonstrate that the MSH system shown in Figs. 3.1(a)-(c) can be adiabatically tuned between 1D and 2D without undergoing a phase transition. To this end, we present in Fig.3.2 the Chern number density for different chain lengths, ranging from an island without chain [Fig. 3.2 (a)], to islands with chain lengths $L = 10$ [Fig. 3.2 (b)] and $L = 20$ [Fig. 3.2 (c)]. Throughout this evolution, $C(\mathbf{r})$ not only remains close to -1 inside the Shiba island, but the end of the chains also exhibits some non-zero negative value for $C(\mathbf{r})$, again demonstrating the adiabatic evolution of the MSH structure. Thus, the results shown in Figs. 3.1 and 3.2 demonstrate that it is not only possible to adiabatically tune between 1D and 2D topological superconductivity via atomic manipulation (and hence spatially separate Majorana fermions without the creation of magnetic vortices [7]), but also to design a single system exhibiting both localized and dispersive Majorana zero modes.

The above results open a new paths to the long sought goal for identifying the topological invariant — the Chern number — through measurements, as attaching chains to a magnetic island via atomic manipulation allows one to count the Chern number. To demonstrate this, we attach a second chain to the island–chain hybrid system of Fig. 3.1(c), and present the resulting lowest energy LDOS in Fig. 3.3(a). As expected, we find that by attaching a second chain, the dispersive Majorana mode moves from the edge of the Shiba island [see Fig. 3.1(c)] to the end of the second chain where it forms a bound state. Thus, attaching two chains to a Shiba island that is in a topological phase with $C = \pm 1$ relocates the zero-energy Majorana modes from the edge of the island to the end of the chains, as shown in Fig. 3.3(a). Coincidentally, this result also demonstrates that the localization of Majorana modes at the end of a chain is insensitive to the particular shape of the chain in its middle. Next, we consider a Shiba island that is in a topological superconducting phase with Chern number $C = 2$, implying that the island possesses two degenerate chiral Majorana edge modes. We note that these two modes are topologically protected from combining into a complex Dirac fermion [23], due to the absence of any coupling between them. When two chains are attached to such an island with $C = 2$, one of the Majorana modes is separated into two zero energy Majorana fermions which are located

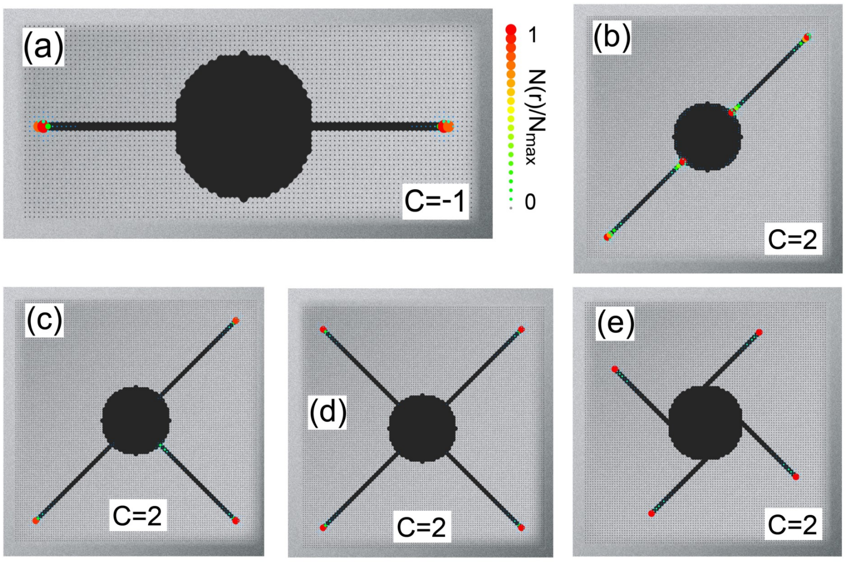

Figure 3.3: (a) LDOS of the lowest energy Majorana mode for a Shiba island with $C = -1$ and two chains of length $L = 30a_0$ attached (same parameters as in Fig. 3.1). (b)-(e) MSH structure with $C = 2$ and parameters $(\mu, \Delta, \alpha, J) = (-0.5t, 0.7t, 0.45t, 2t)$. Lowest energy LDOS for a Shiba island with radius $R = 15a_0$ and with (b) two, (c) three, and (d) four chains of length $L = 30a_0$ attached. (e) The points where the chains are attached are rotated by 45° from (d).

at each of the ends of the two chains, as shown in Fig. 3.3(b) [we note that for this particular set of parameters, the chains are only in a topological phase when they are oriented along the diagonal, but not when they are oriented along the bond directions, which is opposite to the case considered in Fig. 3.1]. At the same time, the second Majorana mode remains localized along the edge of the Shiba island, with large spectral weight concentrated at those points along the edge where the chains are attached. This result is qualitatively different from the $C = -1$ case where in the presence of two chains, no low-energy Majorana mode remains along the edge of the Shiba island [see Fig. 3.3(a)]. When a third chain is attached to the island [see Fig. 3.3(c)], the second Majorana mode is spatially split into two Majorana fermions, one that is located at the end of the third chain, and one that remains located along the edge of the island. Only when four chains are attached to the island [Fig. 3.3(d)] we find that four zero-energy Majorana fermions (arising from the two lowest energy Majorana modes of the island) are located at the end of the chains, with no mode remaining along the edge of the island. We note that this result does not depend on the particular locations where the chains are attached to the island. This is shown in Fig. 3.3(e), being a variant of the geometry in Fig. 3.3(d).

The results shown in Figs. 3.1(c),(d) and Fig. 3.3 suggest a new real space approach to detecting the Chern number of a two-dimensional topological superconductor through atomic manipulation: if spectral weight for a zero-energy state remains located at the edge of the island when $N-1$ chains are attached, but vanishes for N chains, then the Chern number of the 2D topological superconductors is given by $C = N/2$. Our results also imply that by attaching chains to the island, one can effectively change the number of Majorana zero modes in the island, and in particular tune the island to possess an odd number of zero-energy Majorana modes.

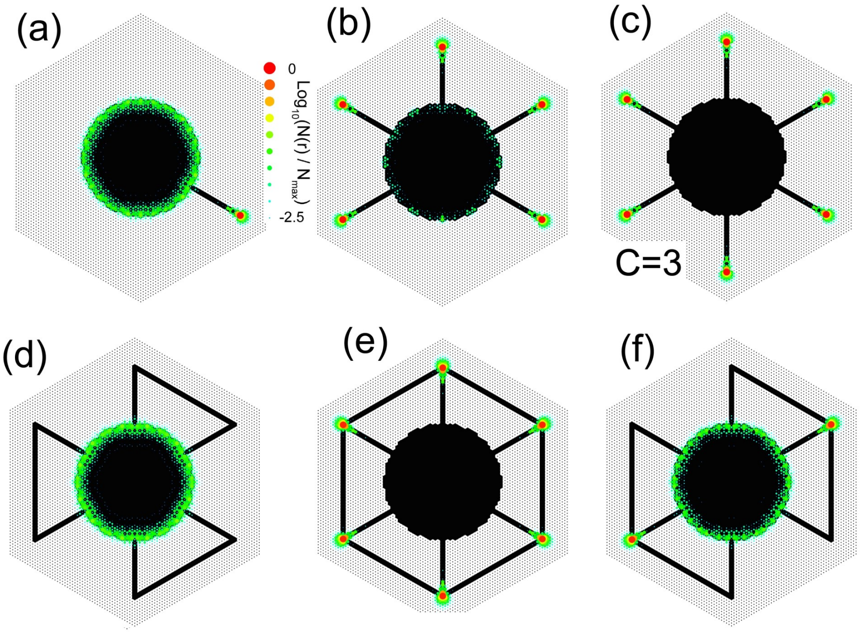

Figure 3.4: Shiba island with radius $R = 20a_0$ on a triangular lattice with parameters $(\mu, \Delta, \alpha, J) = (0.4, 1.2, 0.45, 2.6)t$ yielding a topological phase with $C = 3$. Zero energy LDOS for the island with (a) one, (b) five and (c) six chains of length $L = 20a_0$ attached. Zero energy LDOS for the island with (d) the ends of two neighboring chains connected, giving rise to a windmill-like structure and junctions with an even number of chains (even junction), (e) the ends of neighboring chains connected, giving rise to a spiderweb-like structure and junctions with an odd number of chains (odd junction), and (f) the ends of two opposite chains connected with the ends of their two neighboring chains giving rise to a tie fighter-like structure with both even and odd junctions.

To demonstrate that these findings also hold for higher Chern numbers and different lattice structures, we next consider a Shiba island in the $C = 3$ phase located on a triangular lattice, and present in Figs. 3.4(a)-(c) the resulting lowest-energy LDOS for an increasing number of chains. Such an island possesses 3 degenerate Majorana modes, or 6 Majorana fermions. As expected, we find that with each added chain, a Majorana fermion is removed from the Shiba island and relocated to the end of the chain, leading to a decrease in the spectral weight around the edge of the island, as shown in Figs. 3.4(a),(b). When six chains are attached to the island, all low-energy Majorana modes are removed from the edge of the island [Fig. 3.4(c)]. These results again fully support the validity of the real space approach to counting the Chern number introduced above, as for $N = 6$ chains no zero-energy spectral weight remains around the edge of the island, implying that it is in the $C = N/2 = 3$ phase.

Atomic manipulation can be employed to further tune the location of the Majorana fermions between the end of the chains and the edge of the island. For example, connecting the ends of two neighboring chains by another chain – giving rise to the windmill-like structure shown in Fig. 3.4(d) – leads to junctions where an even number of chains meet (even junctions). Such junctions cannot sustain the existence of Majorana fermions [79], such that all Majorana fermions are relocated back to the edge of the Shiba island. On the other hand, connecting the ends of all chains with ends of their nearest neighbor chains [see Fig. 3.4(e)] gives rise to six junctions where an odd number of chains meet (odd junctions). Such junctions can sustain the existence of a Majorana fermion, such that all Majorana fermions remain located at the end of the chains, i.e., at the junctions. Finally, connecting the ends of two opposite chains with the ends of their two neighboring chains – leading to the tie fighter-like structure shown in Fig. 3.4(f) – produces 4 even and 2 odd junctions, such that 4 Majorana fermions are relocated to the edge of the island, and 2 Majorana fermions remain located at the odd junctions.

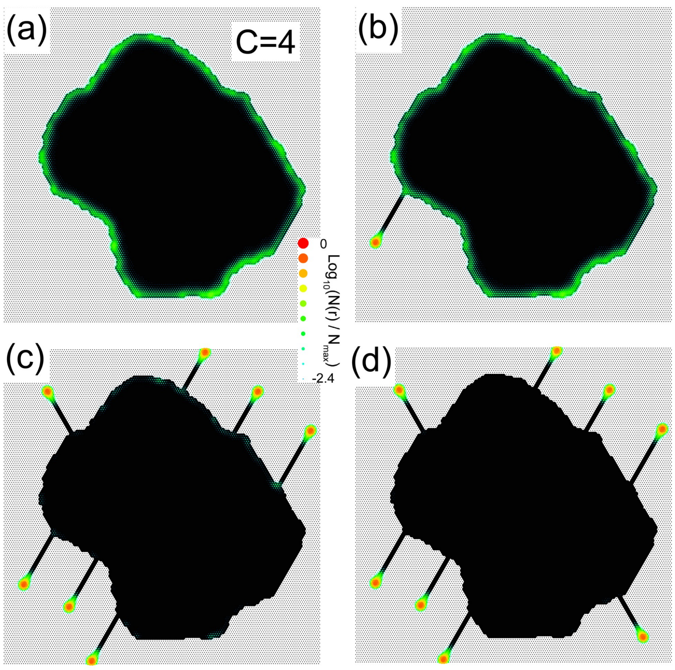

Figure 3.5: Experimentally realized Fe/Re-O(2 $\times$ 1) MSH structure (see Ref. [26]) with $C = 4$. LDOS of zero-energy Majorana modes with (a) no attached chain, (b) one, (c) seven, and (d) eight attached chains. Hamiltonian and parameters for this 10-band model are given in the supplemental material of Ref. [26] and appendix 3.3.

To demonstrate that dimensional tuning and real space counting of Chern numbers can also be achieved in experimentally relevant MSH structures, we consider the MSH structure described by the 10-band model that was employed in the previous chapter to explain the emergence of topological superconductivity in Fe islands deposited on a Re(0001)-O(2x1) surface. The Fe island considered below possesses the same form and spatial extent as the experimentally studied one [26]. However, while the experimentally observed island is in a topological phase with $C = 20$, we have slightly altered the parameters to tune the island into a topological phase with a smaller Chern number of $C = 4$. In this case, the above counting argument predicts that only 8 chains need to be attached to the island remove all zero-energy Majorana fermions from the edge of the island, rather than the 40 chains required in the $C = 20$ phase.

As the island is in the $C = 4$ topological phase, it exhibits four chiral Majorana modes along the edge of the island, with the corresponding $E = 0$ LDOS shown in Fig. 3.5 (a). As before we find that a single chain of magnetic adatoms attached to the island, possesses a Majorana bound state that is localized at the end of the chain, with all other Majorana fermions remaining localized along the edge of the island, as follows from the zero-energy LDOS shown in Fig. 3.5(b). For an island with 7 chains attached [see Fig. 3.5(c)], substantial spectral weight has been removed from the edge of the island as 7 Majorana bound states are now located at the end of the chains, with only a single chiral Majorana fermion remaining located along the edge of the island. We note that as expected the integrated spectral weight along the edge of the island is the same as that around each end of the chains. However, as the spectral weight of the Majorana fermion is extended over the entire length of the edge, the peak intensity in the LDOS along the edge is significantly smaller than that at the end of the chains [see Fig. 3.5(c)]. Finally, adding an 8th chain to the island relocates the last Majorana fermion to the end of the chain, leading to a vanishing zero-energy LDOS at the edge of the island [Fig. 3.5 (d)]. We therefore conclude that proposed real space approach to counting the Chern number holds even for experimentally relevant MSH structures, thus further supporting its validity.

The above results also suggest how the dimensional tuning of Majorana fermions between 1D and 2D can be generalized to MSH structures with Chern numbers different from $C = \pm 1$ which was discussed in Fig. 3.1. Specifically, we find that it is possible to use atomic manipulation techniques to adiabatically tune between a Shiba island with $|C|$ chiral Majorana modes, and a network of chains that host $2|C|$ localized Majorana bound states, as shown in Figs. 3.1(g), 3.3(c), 3.4(c),(d) and 3.5(d). Atomic manipulation techniques thus provide a promising new approach to the quantum engineering of Majorana fermions.

3.3 Parameters for the Fe/Re-O(2×1) MSH structure

To reduce the Chern number from experimentally relevant case of $C = 20$ for experimentally realized Fe/Re-O(2×1) structure in Ref. [26] to $C = 4$ discussed in Fig. 3.5, the following parameters were changed from those given in the supplemental material of Ref. [26]: $\Delta_{Re} = 33$ meV, $\mu_{Fe} = -10.96$ meV, $\lambda_{Fe} = 0.64$ meV, $\alpha_{Fe} = 3.36$ meV, and $\Delta_{Fe} = 3.28$ meV.

Chapter 4

Topological Surface Superconductivity in $FeSe_{1-x}Te_x$

This chapter investigates a new possibile explanation for the modeling of topological superconductivity in $FeSe_{0.45}Te_{0.55}$, in which we extend a previous model of $FeSe_{0.45}Te_{0.55}$ to include both surface magnetism and Rashba spin-orbit coupling. By then calculating the phase diagram over a range of magnetism strengths and global chemical potentials, we demonstrate the existence of a range of topological phases in this model. We then use a generic model of $s_{\pm}$-wave superconductivity to calculate the local density-of-states (LDOS) as an STS moves across a vortex in both a topological and trivial superconductor. We find that only in the topological case is there a zero-energy state, a Majorana zero mode (MZM). Additionally, this MZM is strongly spin-polarized providing a strong spectroscopic indicator for experimentalists verifying the existence of such MZMs.

4.1 Model

To investigate the emergence of topological superconductivity on the surface of $FeSe_{1-x}Te_x$, we consider a 5-orbital model extracted from an analysis of STS experiments on clean $FeSe_{1-x}Te_x$ [80, 81]. In addition, we include in this model (a) the effects of surface magnetism, evidence for which was recently reported by ARPES experiments [82], through an exchange field, and (b) a Rashba spin orbit interaction that arises from the breaking of the inversion symmetry on the surface, yielding the real-space Hamiltonian $H = H_0 + H_{SC}$, with

$$
\begin{aligned}
H_0 = &- \sum_{\mathbf{r},\mathbf{r}',\sigma} \sum_{\beta,\gamma=1}^{5} t^{\beta\gamma}_{\mathbf{r},\mathbf{r}'} c^\dagger_{\mathbf{r},\beta,\sigma} c_{\mathbf{r}',\gamma,\sigma} + i\alpha \sum_{\mathbf{r},\mathbf{r}',\sigma,\sigma'} \sum_{\beta=1}^{5} c^\dagger_{\mathbf{r},\sigma,\beta} \left(\hat{\boldsymbol{\delta}} \times \boldsymbol{\sigma}\right)^z_{\sigma\sigma'} c_{\mathbf{r}+\hat{\boldsymbol{\delta}},\sigma',\beta} \\
&+ J \sum_{\mathbf{r},\mathbf{r}',\sigma,\sigma'} \sum_{\beta=1}^{5} \mathbf{S}_{\mathbf{R}} \cdot c^\dagger_{\mathbf{R},\sigma,\beta} \boldsymbol{\sigma}_{\sigma\sigma'} c_{\mathbf{R},\sigma,\beta} + \mu \sum_{\mathbf{r},\mathbf{r}',\sigma} \sum_{\beta=1}^{5} c^\dagger_{\mathbf{r},\beta,\sigma} c_{\mathbf{r},\beta,\sigma} + \text{H.c.}
\end{aligned} \tag{4.1}
$$

$$
H_{SC} = - \sum_{\langle \mathbf{r},\mathbf{r}' \rangle} \sum_{\beta=1}^{5} I^{\beta}_{\mathbf{r},\mathbf{r}'} \; c^\dagger_{\mathbf{r},\beta,\uparrow} c^\dagger_{\mathbf{r}',\beta,\downarrow} c_{\mathbf{r},\beta,\downarrow} c_{\mathbf{r}',\beta,\uparrow} \; . \tag{4.2}
$$

Here $\alpha, \beta = 1, ..., 5$ are the orbital indices corresponding to the d_{xz}-, d_{yz}-, $d_{x^2-y^2}$-, d_{xy}-, and $d_{3z^2-r^2}$-orbitals, respectively, $-t^{\alpha\beta}_{\mathbf{r},\mathbf{r}'}$ represents the electronic hopping amplitude between orbital β at site $\mathbf{r}$ and orbital γ at site $\mathbf{r}'$, $c^\dagger_{\mathbf{r},\alpha,\sigma}(c_{\mathbf{r},\alpha,\sigma})$ creates (annihilates) an electron with spin σ at site $\mathbf{r}$ in orbital α, $i\alpha$ represents the Rashba spin-orbit interaction amplitude, μ represents a global chemical potential, and $\boldsymbol{\sigma}$ is the vector of spin Pauli matrices. Due to the full superconducting gap, which suppresses Kondo screening, we consider the magnetic moments to be static in nature, such that $\mathbf{S}_{\mathbf{R}}$ is a classical vector representing the direction of the surface atom's spin located at $\mathbf{R}$, and J is its exchange coupling with the conduction electron spin. The opening of a gap at the Dirac point, assuming a helical spin-structure of the Dirac cone, implies that the magnetic moments are aligned perpendicular to the surface, such that for concreteness, we assume an out-of-plane ferromagnetic alignment. To obtain a superconducting order parameter with $s_\pm$-wave symmetry [83], we take H_{SC} to describe superconducting intra-orbital pairing between next-nearest neighbor Fe sites (in the 2 Fe unit cell, Fig. 4.1), with $I^{\alpha}_{\mathbf{r},\mathbf{r}'}$ being the pairing interaction. Using a mean-field decoupling of H_{SC}, we obtain

$$
H^{MF}_{SC} = \sum_{\langle \mathbf{r},\mathbf{r}' \rangle} \sum_{\beta=1}^{5} \Delta_{\beta\beta} c^\dagger_{\mathbf{r},\beta,\uparrow} c^\dagger_{\mathbf{r}',\beta,\downarrow} + H.c. \tag{4.3}
$$

To obtain the topological phase diagram, we compute the Chern number using eqn. 2.24.

4.2 Phase diagram

In Fig. 4.2(a) we present the resulting phase diagram for $\alpha = 7$ meV, as a function of μ and J. We here restrict our attention to $\mu > 0$ to preserve the topology of the Fermi surfaces, ensuring

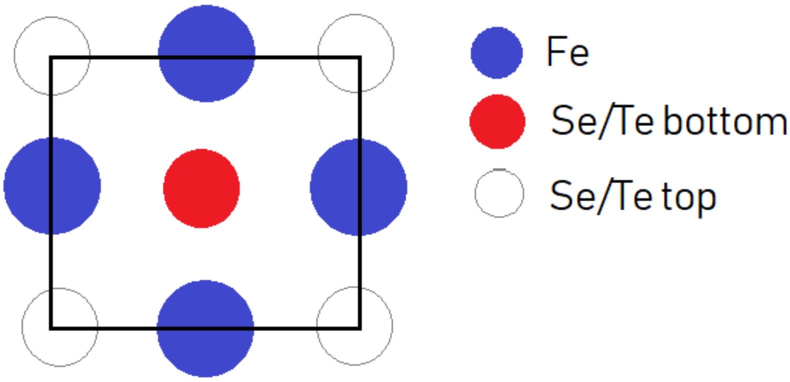

Figure 4.1: The 2 Fe unit cell for $FeSe_{0.45}Te_{0.55}$

that the Fermi surfaces remain closed around the Γ and X/Y-points and that the system still exhibits a full $s_{\pm}$-wave SC gap. As we can see in Fig. 4.2(b) and (c), both the C=2, -3 phases preserve this Fermi surface topology and maintain the full SC gap. Interestingly enough, we find that already for small exchange interactions of J of the order of a few meV, a variety of topological phases exist. Specifically phases for $C = -3, -2, -1, 1$ can all be found over the range of the diagram. The grey region in the upper left hand corner is the region in which the Fermi surface touches the nodal lines of the superconducting order parameter, causing the gap to close and thus destroy the topological order.

4.3 MZM in a vortex core

The detailed spatial, energy and spin-structure of MZMs inside vortex cores [29, 30] provides another clue as to the potential origin of topological superconductivity in $FeSe_{0.45}Te_{0.55}$. Due to the large number of orbitals per site, the self-consistent calculation of a vortex in the full $FeSe_{0.45}Te_{0.55}$ model is computationally too demanding. We have therefore consider a simplified model for a topological $s_{\pm}$-wave superconductor, given by the Hamiltonian

$$\begin{aligned}\mathcal{H} = -t \sum_{\mathbf{r},\mathbf{r}',\sigma} c^{\dagger}_{\mathbf{r},\sigma} c_{\mathbf{r}',\sigma} - \mu \sum_{\mathbf{r},\sigma} c^{\dagger}_{\mathbf{r},\sigma} c_{\mathbf{r},\sigma} + \sum_{\langle\langle \mathbf{r},\mathbf{r}'\rangle\rangle} \Delta_0 c^{\dagger}_{\mathbf{r},\uparrow} c^{\dagger}_{\mathbf{r}',\downarrow} + i\alpha \sum_{\mathbf{r},\sigma\sigma'} c^{\dagger}_{\mathbf{r},\sigma} \left(\hat{\boldsymbol{\delta}} \times \boldsymbol{\sigma}\right)^{z}_{\sigma\sigma'} c_{\mathbf{r}+\hat{\boldsymbol{\delta}},\sigma'} \\ + \sum_{\mathbf{r},\sigma,\sigma'} c^{\dagger}_{\mathbf{r},\sigma} (\mathbf{S}_{\mathbf{r}} \cdot \boldsymbol{\sigma})_{\sigma\sigma'} c_{\mathbf{r},\sigma'} + H.c. \ ,\end{aligned} \tag{4.4}$$

where $-t$ is the hopping amplitude between nearest neighbor sites on a triangular lattice, μ is the chemical potential, and Δ_0 is the superconducting $s_{\pm}$-wave order parameter. J is the

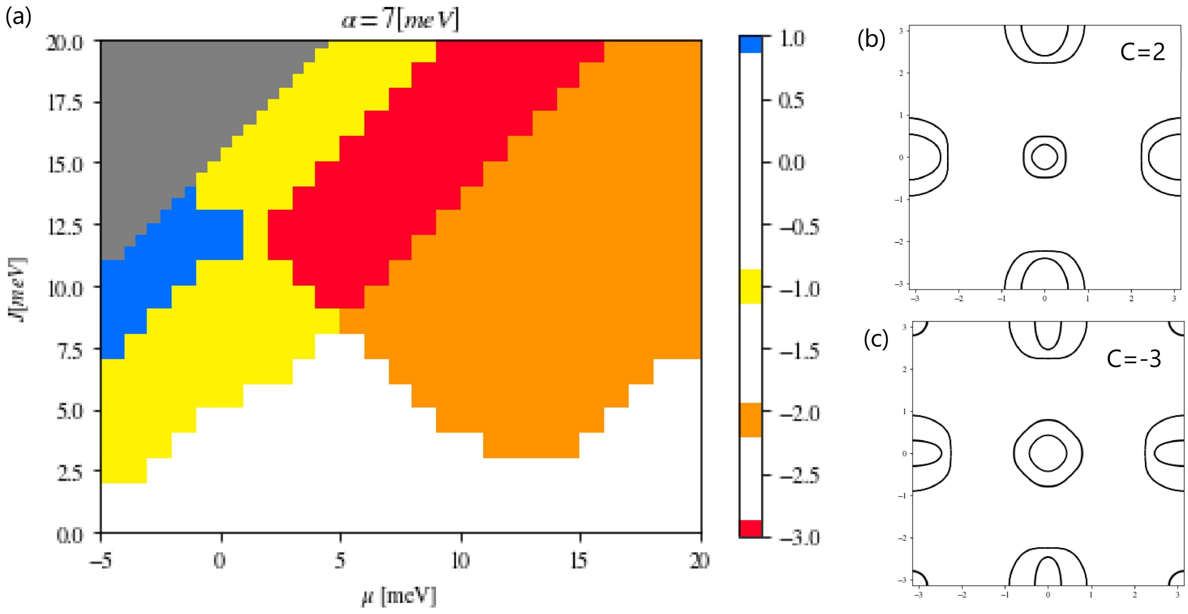

Figure 4.2: (a) Topological phase diagram of $FeSe_{0.45}Te_{0.55}$ in the $(\mu - J)$-plane with $\alpha = 7$ meV. Inside the greyed out region, the gap is closed and there is no topological order. Fermi surfaces in the (b) $C = 2$ and (c) $C = -3$ phases.

magnetic exchange coupling, and $c^{\dagger}_{\mathbf{r},\sigma}$ creates an electron with spin σ at site $\mathbf{r}$. $\mathbf{S_r}$ represents the magnetic moment's spin S at site $\mathbf{r}$. $\langle\langle \mathbf{r}, \mathbf{r}' \rangle\rangle$ denotes a sum over next nearest-neighbor sites.

In Fig. 4.3(a) we present the self-consistently computed superconducting order parameter near a vortex core in a topological superconducting phase with $C = 1$. A linecut of the LDOS through the vortex core shown in Fig. 4.3(b) shows the presence of a zero-energy state, which we associate with the MZM, mirroring recent experimental results [29]. This conclusion is supported by the fact that a zero-energy state in a vortex core is absent when the superconductor is in the trivial phase, as shown in Fig. 4.3(c).

In addition to the MZM, the LDOS near the vortex core reveals trivial Caroli-de Gennes-Matricon (CdGM) in-gap states which show a characteristic energy dependence with distance from the vortex core. The observation of these CdGM states in our model closely matches recent experimental results [84]. These trivial states are also present in the topological trivial phase, as shown in Fig. 4.3(d). Of particular interest is the spin structure of the MZM: a plot of the spin-resolved LDOS shown in Fig. 4.3(c) reveals that the MZM is strongly spin-polarized. Interestingly enough, the two spin-components are out-of-phase: the spin-$\uparrow$ LDOS exhibits a maximum, where the spin-$\downarrow$ LDOS vanishes, and vice versa. This strong spin-polarization of the MZM is a direct consequence of the surface magnetism, and hence a characteristic signature of the here proposed origin of the topological superconductivity in $FeSe_{0.45}Te_{0.55}$, in stark contrast to the previously proposed origin in the presence of a bulk topological insulator that does not break the time-reversal invariance.

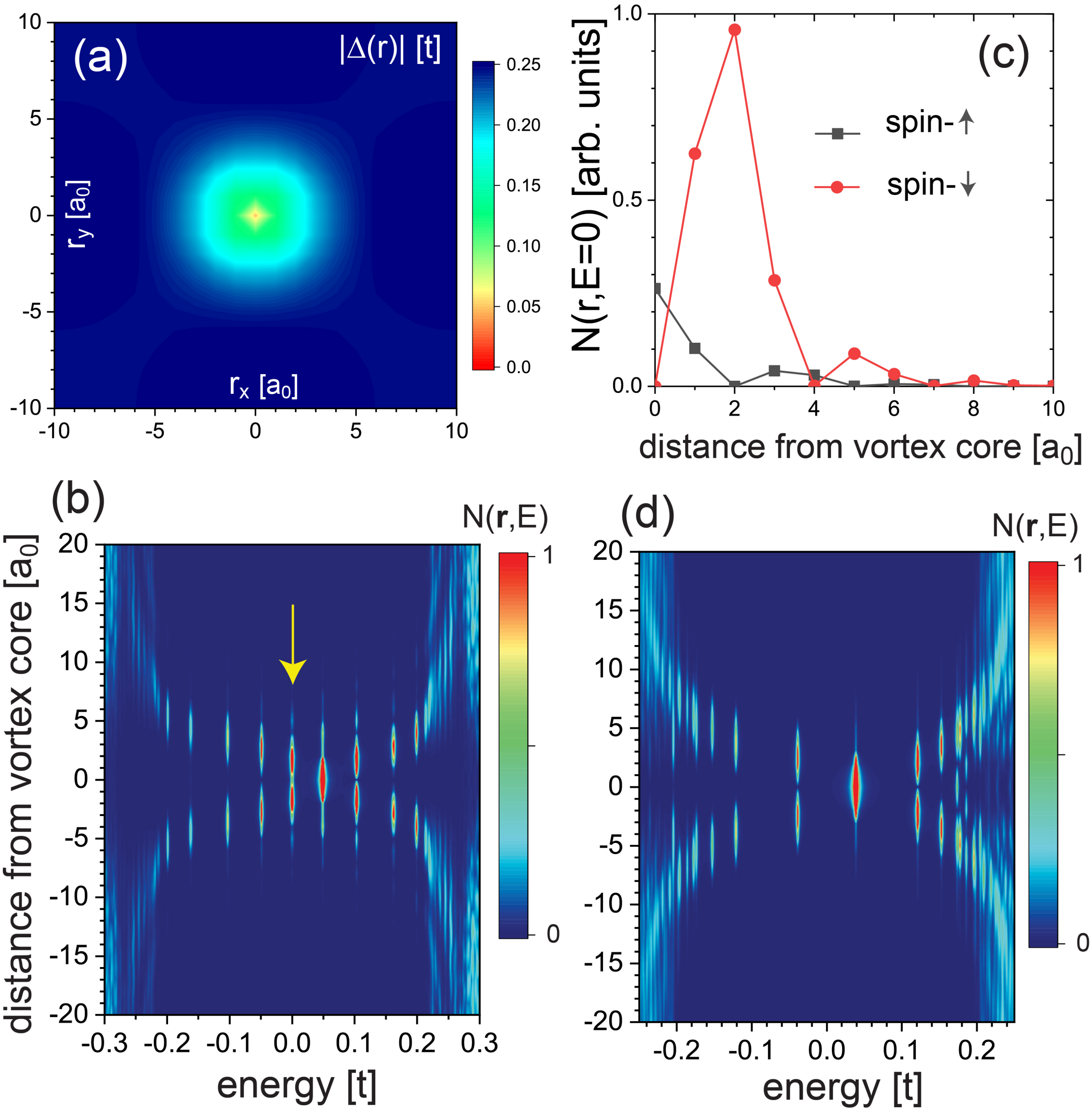

Figure 4.3: Linecut of the LDOS, $N(\mathbf{r}, E)$, through the center of the vortex core for in the (a) topological phase with $(\mu, J, \alpha, \Delta) = (-5, 1.7, 0.625, 0.25)t$ yielding $C = 1$ (the MZM is indicated by a yellow arrow), and (b) the trivial phase with $(\mu, J, \alpha, \Delta) = (-4, 0.8, 0.25, 0.25)t$.

Chapter 5

Scanning Tunneling Shot Noise Spectroscopy in Kondo systems

This work was previously published as "Scanning tunneling shot-noise spectroscopy in Kondo systems" S. Cocklin and D. K. Morr *Physical Review B* 100, 125146, 2019.

As we have seen in the previous chapters, STS is a powerful probe for understanding real-space properties of condensed matter systems. A further extension of STS for investigating such systems is scanning tunneling shot noise spectroscopy (STSNS). In a demonstration of the use of this probe, we theoretically examine the shot noise for one well-studied, well-understood, correlated electron system, namely Kondo systems.

In this chapter, we will investigate the relation between the bias dependence of the current, the differential conductance, the zero-frequency shot-noise, and the Fano factor, defined as

$$F = \frac{S(\omega = 0)}{2e|I|} \tag{5.1}$$

around magnetic adatoms located on metallic surfaces exhibiting a Kondo effect, as well as in Kondo lattices, as observed by scanning tunneling shot noise spectroscopy. We will show that the Fano factor exhibits a characteristic lineshape that reflects not only the strong correlations arising from Kondo screening, but also quantum interference effects due to multiple tunneling paths. This characteristic lineshape of F is not unlike the Kondo resonance observed in the differential conductance (for example in ref. [40]), and presents an additional test for our understanding of the Kondo effect.

The rest of this chapter is organized as follows. In Sec. 5.1 we present our theoretical model and derive the form of the current and shot-noise measured by an STS tip. This model was previously employed to successfully describe the Kondo resonance of a Co adatom located on a Au(111) surface. In Sec. 5.2 we discuss our results for the shot noise around a single magnetic adatom, the relation between the differential conductance and the shot noise lineshape, and the effects of tunneling interference. Finally, in Sec. 5.3 we discuss the form of the shot noise and Fano factor in Kondo lattice systems.

5.1 Theoretical Model

We begin by discussing the model for the current and shot noise around a single Kondo impurity. To study the properties of a single Kondo impurity, we employ the theoretical model of Ref. [43] which was used to successfully describe the lineshape of the Kondo resonance in the differential conductance, dI/dV, measured around a single magnetic Co adatom located on a metallic Au(111) surface [37]. Such a system is described by the Hamiltonian [36]

$$\hat{H} = -\sum_{\mathbf{r},\mathbf{r}',\sigma} t_{\mathbf{r}\mathbf{r}'} c^{\dagger}_{\mathbf{r},\sigma} c_{\mathbf{r}',\sigma} + J\mathbf{S}^{K}_{\mathbf{R}} \cdot \mathbf{s}^{c}_{\mathbf{R}} \tag{5.2}$$

where $c^{\dagger}_{\mathbf{r},\sigma}$ ($c_{\mathbf{r},\sigma}$) creates (annihilates) a conduction electron with spin σ at site $\mathbf{r}$ on the Au(111) surface. Here, $t_{\mathbf{r}\mathbf{r}'} = 1.3$ eV is the fermionic hopping element between nearest-neighbor sites in the triangular Au(111) surface lattice, and $\mu = -7.34$ eV is its chemical potential. These parameters describe the dispersion of the experimentally observed Au(111) surface state [103] that takes part in the Kondo screening of the Co adatom. Moreover, $J > 0$ is the Kondo coupling, and $\mathbf{S}^{K}_{\mathbf{R}}$ and $\mathbf{s}^{c}_{\mathbf{R}}$ are the spin operators of the magnetic Co adatoms and the conduction electron at site $\mathbf{R}$, respectively.

To describe the Kondo screening of the Co adatom by the two-dimensional Au(111) surface state, we employ a large-N expansion [104–110]. Here, $\mathbf{S}^{K}_{\mathbf{R}}$ is generalized to $SU(N)$ and represented via Abrikosov pseudofermions $f^{\dagger}_{m}, f_{m}$ which obey the constraint $\sum_{m=1..N} f^{\dagger}_{m} f_{m} = 1$ with $N = 2S+1$ being the spin degeneracy of the magnetic adatom. This constraint is enforced by means of a Lagrange multiplier ε_f, while the exchange interaction in Eq.(5.2) is decoupled via the hybridization field, s. The hybridization represents the hopping between the conduction electron states and the pseudofermion f-electron states with the resulting Kondo temperature

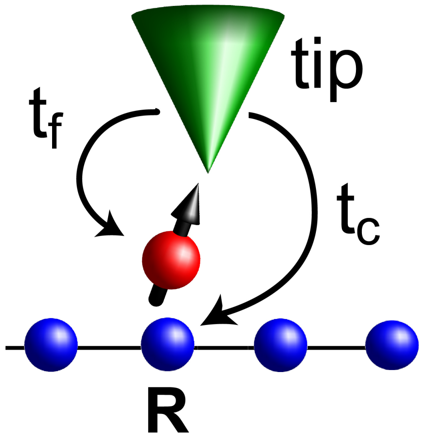

Figure 5.1: Paths of electrons tunneling from the STS tip either into the conduction band or into the magnetic level of the Kondo impurity, with tunneling amplitudes t_c and t_f, respectively.

scaling as [105], $T_K \sim s^2$. For fixed J, ε_f and s are obtained on the saddle point level by minimizing the effective action [108]. Finally, the tunneling of electrons from the STS tip into the system is described by the Hamiltonian

$$\hat{H} = \sum_{\sigma} t_c c^{\dagger}_{\mathbf{R},\sigma} d_\sigma + t_f f^{\dagger}_{\mathbf{R},\sigma} d_\sigma + H.c. \tag{5.3}$$

where t_c (t_f) are the amplitudes for tunneling of electrons from the tip into the Au(111) surface band (the magnetic f-level), as schematically shown in Fig. 5.1, and d_σ annihilates a fermion in the STS tip.

To compute the current and associated shot-noise measured by the STS tip, we employ the non-equilibrium Keldysh Greens function formalism [111, 112]. Unless otherwise stated, all results presented in Sec. 5.2 were obtained at zero temperature. When the STS tip is positioned above the magnetic adatom at site $\mathbf{R}$, the current flowing from the STS tip into the system is given by [113]

$$I_{\mathbf{R}}(V) \quad = \quad -\frac{2e}{\hbar} \mathrm{Re} \int_0^V \frac{d\omega}{2\pi} \left[t_c \hat{G}^{<}_{12}(\omega) + t_f \hat{G}^{<}_{13}(\omega) \right] \,, \tag{5.4}$$

with the full lesser Greens function matrix given by

$$
\begin{aligned}
\hat{G}^{<}(\omega) &= [\hat{1} - \hat{g}^r(\omega)\hat{t}]^{-1}\hat{g}^{<}(\omega)[\hat{1} - \hat{t}\hat{g}^a(\omega)]^{-1} \ ; \\
\hat{g}^{<}(\omega) &= -2i\hat{n}_F(\omega)\mathrm{Im}\,[\hat{g}^r(\omega)] \ ; \\
\hat{g}^r(\omega) &= \begin{pmatrix} g_t^r(\omega) & 0 & 0 \\ 0 & g_{cc}^r(\mathbf{R},\mathbf{R},\omega) & g_{cf}^r(\mathbf{R},\mathbf{R},\omega) \\ 0 & g_{fc}^r(\mathbf{R},\mathbf{r},\omega) & g_{ff}^r(\mathbf{R},\mathbf{R},\omega) \end{pmatrix} \ .
\end{aligned} \tag{5.5}
$$

Here, $\hat{t}$ is the symmetric hopping matrix with non-zero elements $\hat{t}_{12} = t_c$, $\hat{t}_{13} = t_f$. $\hat{n}_F$ is diagonal containing the Fermi-distribution functions of the tip, $n_F^t(\omega)$, and of the f- and c-electron states, $n_F(\omega)$. g_t^r is the retarded Greens function of the tip, and $g_{\alpha\beta}(\mathbf{r'},\mathbf{r},\tau) = -\langle T_\tau \alpha_{\mathbf{r'}}(\tau)\beta_{\mathbf{r}}^\dagger(0)\rangle$ $(\alpha, \beta = c, f)$ describes the many-body effects arising from the hybridization of the conduction band with the f-electron level, and the concomitant screening of the magnetic moment, with

$$
\begin{aligned}
g_{ff}^r(\mathbf{R},\mathbf{R},\omega) &= \left[\omega - \varepsilon_f - s^2 g_0^r(\mathbf{R},\mathbf{R},\omega)\right]^{-1} \ ; \\
g_{cc}^r(\mathbf{R},\mathbf{R},\omega) &= \left\{[g_0^r(\mathbf{R},\mathbf{R},\omega)]^{-1} - \frac{s^2}{\omega - \varepsilon_f + i\delta}\right\}^{-1} \\
g_{cf}^r(\mathbf{R},\mathbf{R},\omega) &= g_0^r(\mathbf{R},\mathbf{R},\omega) s g_{ff}^r(\mathbf{R},\mathbf{R},\omega) \ ,
\end{aligned} \tag{5.6}
$$

where g_0^r is the retarded Greens function of the unhybridized conduction electron band. For a more in-depth discussion, see Ref. [44].

It is instructive to consider the weak-tunneling limit ($t_c, t_f \to 0$) of the current by expanding Eq.(5.4) up to second order in the tunneling amplitudes, in which case one obtains from Eq.(5.4)

$$
I_{\mathbf{R}}(V) = -\frac{4\pi e}{\hbar}\pi N_t \int_{-\infty}^{\infty} \frac{d\epsilon}{2\pi} \left[n_F^t(\epsilon) - n_F(\epsilon)\right] \times \left[t_c^2 \mathrm{Im} g_{cc}^r(\epsilon) + 2t_c t_f \mathrm{Im} g_{cf}^r(\epsilon) + t_f^2 \mathrm{Im} g_{ff}^r(\epsilon)\right]
$$

where all $g_{\alpha,\beta}^r$ $(\alpha, \beta = c, f)$ are the local retarded Greens' functions at the site of the magnetic adatom, and N_t is the density of states on the tip. We previously demonstrated [43] that the experimental dI/dV lineshape measured at the site of a Co adatom on a Au(111) surface [37] can be described by computing the differential conductance from Eq.(5.7) using the parameters $J = 1.39$ eV, $t_f/t_c = -0.066$, and $N = 4$.

We next consider the shot-noise which is defined as the current-current correlation function [90, 91]

$$S(t,t') = \langle\{\delta I(t), \delta I(t')\}\rangle = \langle\{I(t), I(t')\}\rangle - 2\langle I\rangle^2 \ . \tag{5.7}$$

We then obtain for the zero frequency noise $S_0 = S(\omega = 0)$ at the site of the adatom

$$\begin{aligned} S_0 = 2\left(\frac{ie}{\hbar}\right)^2 \int_{-\infty}^{\infty} \frac{d\epsilon}{2\pi} & t_c^2\{2G^>_{dc}(\epsilon)G^<_{dc}(\epsilon) - G^>_{dd}(\epsilon)G^<_{cc}(\epsilon) - G^<_{dd}(\epsilon)G^>_{cc}(\epsilon)\} \\ & +2t_c t_f\{G^>_{df}(\epsilon)G^<_{dc}(\epsilon) + G^<_{df}(\epsilon)G^>_{dc}(\epsilon) - G^>_{dd}(\epsilon)G^<_{fc}(\epsilon) - G^<_{dd}(\epsilon)G^>_{fc}(\epsilon)\} \\ & +t_f^2\{2G^>_{df}(\epsilon)G^<_{df}(\epsilon) - G^>_{dd}(\epsilon)G^<_{ff}(\epsilon) - G^<_{dd}(\epsilon)G^>_{ff}(\epsilon)\} \end{aligned} \tag{5.8}$$

where all Greens functions in Eq.(5.8) are local Greens function at the site of the adatom.

Considering again the weak-tunneling limit $t_c, t_f \to 0$, the expression for the shot noise in Eq.(5.8) up to second order in the tunneling amplitudes simplifies to

$$\begin{aligned} S_0 = -8\pi\left(\frac{e}{\hbar}\right)^2 N_T \int_{-\infty}^{\infty} \frac{d\epsilon}{2\pi} & \left\{\left[1 - n_F^T(\epsilon)\right] n_F(\epsilon) + \left[1 - n_F(\epsilon)\right] n_F^T(\epsilon)\right\} \\ & \times \left[t_c^2 \mathrm{Im} g^r_{cc}(\epsilon) + 2t_c t_f \mathrm{Im} g^r_{cf}(\epsilon) + t_f^2 \mathrm{Im} g^r_{ff}(\epsilon)\right] \end{aligned} \tag{5.9}$$

By comparing the expressions for the current, Eq.(5.7), and shot-noise, Eq.(5.9) in the weak-tunneling limit, i.e., up to second order in the tunneling amplitudes, we find that at zero temperature the Fano factor, Eq.(5.1), is given by $F = 1$, implying that the noise is Poissonian. However, the inclusion of higher order tunneling terms in the calculation of the current and shot-noise using Eqs.(5.4) and (5.8) respectively, yields not only deviations of F from the Poissonian limit, but also a characteristic bias dependence, that similar to the differential conductance, reflects the Kondo screening process, as shown below. Finally, we note that the definition of the Fano factor given in Eq.(5.1) differs from that used in Refs. [97, 100], as Eq.(5.1) involves the total current and noise measured by the STS tip, without any subtraction.

To study the shot noise in Kondo lattice systems, we generalize the Hamiltonian in Eq.(5.2) to

$$\hat{H} = -\sum_{\mathbf{r},\mathbf{r}',\sigma} t_{\mathbf{r}\mathbf{r}'} c^\dagger_{\mathbf{r},\sigma} c_{\mathbf{r}',\sigma} + J\sum_{\mathbf{r}} \mathbf{S}^K_{\mathbf{r}} \cdot \mathbf{s}^c_{\mathbf{r}} + \sum_{\langle\mathbf{r},\mathbf{r}'\rangle} I_{\mathbf{r},\mathbf{r}'} \mathbf{S}^K_{\mathbf{r}} \mathbf{S}^K_{\mathbf{r}'} \tag{5.10}$$

where the sums in the run over all sites $\mathbf{r}$ of the conduction electron lattice. The last term represents the antiferromagnetic interaction between the magnetic moments where we assume that $I_{\mathbf{r},\mathbf{r}'} > 0$ is non-zero for nearest-neighbor sites only. Introducing again an Abrikosov pseudo-fermion representation of $\mathbf{S}^K_\mathbf{r}$, the antiferromagnetic interaction term can be decoupled using $\chi_0 = I\langle f^\dagger_{\mathbf{r},\alpha} f_{\mathbf{r}',\alpha}\rangle$, which is a measure for the strength of the magnetic correlations in the system. With this decoupling, the full Green's functions in momentum space, which describe the hybridization between the c- and f-electron bands, are given by

$$\begin{aligned} g_{ff}(\mathbf{k},\alpha,\omega) &= \left[(g^0_{ff}(\mathbf{k},\alpha,\omega))^{-1} - s^2 g^0_{cc}(\mathbf{k},\alpha,\omega)\right]^{-1} \ ; \\ g_{cc}(\mathbf{k},\alpha,\omega) &= \left[(g^0_{cc}(\mathbf{k},\alpha,\omega))^{-1} - s^2 g^0_{ff}(\mathbf{k},\alpha,\omega)\right]^{-1} \ ; \\ g_{cf}(\mathbf{k},\alpha,\omega) &= -g^0_{cc}(\mathbf{k},\alpha,\omega) s g_{ff}(\mathbf{k},\alpha,\omega) \ , \end{aligned} \tag{5.11}$$

where

$$\begin{aligned} g^0_{cc} &= \frac{1}{\omega + i\delta - \varepsilon^c_\mathbf{k}} \\ g^0_{ff} &= \frac{1}{\omega + i\delta - \varepsilon^f_\mathbf{k}} \\ \varepsilon^f_\mathbf{k} &= -2\chi_0(\cos k_x + \cos k_y) + \varepsilon_f \\ \varepsilon^c_\mathbf{k} &= -2t(\cos k_x + \cos k_y) - \mu_c \ . \end{aligned} \tag{5.12}$$

Here, $\varepsilon^f_\mathbf{k}$ and $\varepsilon^c_\mathbf{k}$ are the dispersions of the unhybridized conduction electron and f-electron bands, respectively. The dispersions of the hybridized conduction and f-electron bands are then given by

$$E^\pm_\mathbf{k} = \frac{\varepsilon^c_\mathbf{k} + \varepsilon^f_\mathbf{k}}{2} \pm \sqrt{\left(\frac{\varepsilon^c_\mathbf{k} - \varepsilon^f_\mathbf{k}}{2}\right)^2 + s^2} \ . \tag{5.13}$$

Finally, we note that the formal expressions for the current and the shot-noise in the Kondo lattice are the same as given in Eqs.(5.4) and (5.8), respectively, with the local Greens functions in Eq.(5.6) being computed via Fourier transform from their momentum space form in Eq.(5.11).

5.2 Shot Noise around a Kondo impurity

We begin by considering the current and shot-noise around a single Kondo impurity, using the parameters previously employed to explain the differential conductance of a Kondo-screened

Co adatom located on a Au(111) surface [37, 43]. While the Fano factor is unity in the weak tunneling limit, i.e., up to second order in the tunneling amplitudes, it deviates from this result with increasing tunneling amplitude t_c, t_f, exhibiting a characteristic lineshape that sensitively depends on the ratio of the tunneling amplitudes t_f/t_c. Thus, in order to be able to measure experimentally a characteristic Fano factor, it is desirable to have large tunneling amplitudes, corresponding to small distances between STS tip and sample and sufficiently large currents.

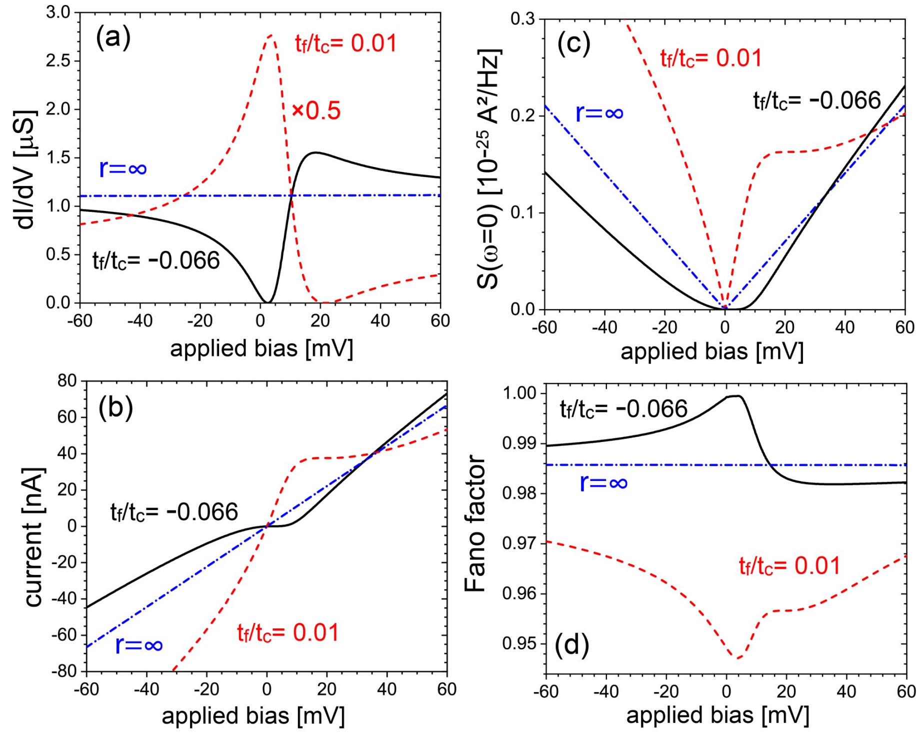

Figure 5.2: (a) dI/dV, (b) current I, (c) noise S_0, and (d) Fano factor F for two different values of $t_f/t_c = -0.066$ and $t_f/t_c = 0$, as well as far removed $r = \infty$ from the Kondo impurity. Results are shown for zero temperature.

While the ratio t_f/t_c can be determined by fitting the experimental dI/dV lineshape, as was done for the case of a Co adatom on a Au(111) surface in Ref. [43], it is difficult to extract the absolute values of the tunneling amplitudes. Therefore, in order to determine whether deviations of F from unity can be observed experimentally, it is necessary to treat t_c, t_f as implicit parameters, and correlate the IV-curves that result from given values for t_c, t_f with the form of the Fano factor. We therefore present below the current, differential conductance and noise in absolute units for different sets of t_c, t_f. We note that increasing t_c with constant t_f/t_c leads to an increase in the current between the tip and the system, and thus corresponds to decreasing the distance between tip and sample in experiments. Current state-of-the-art STS experiments can achieve currents in the tunneling regime of hundreds of nA for bias of a few mV [114, 115], rendering all theoretical results shown below within the experimental accessible region.

Using the same set of parameters as previously employed in Ref. [43], we present in Fig.5.2(a) the differential conductance at the site of a single Kondo impurity for two values of t_f/t_c. For $t_f/t_c = -0.066$, we obtain the dI/dV lineshape that was previously employed to fit the dI/dV lineshape measured above a Co adatom on a Au(111) surface (black line). For comparison addition, we also present dI/dV for $t_f/t_c = +0.01$ (red dashed line), whose lineshape exhibits an asymmetry that is reversed from that obtained for $t_f/t_c = -0.066$, as well as dI/dV away from the adatom at $r = \infty$ (blue dotted-dashed line) which is that of the unhybridized conduction band. To understand the difference in the asymmetry of the dI/dV lineshapes, we consider the IV-curves for these three cases in Fig.5.2(b). We find that the Kondo correlations lead to a suppression of the current for $t_f/t_c = -0.066$ from its value for $r = \infty$, but to an enhancement for $t_f/t_c = +0.01$. This in turn accounts for the change in the asymmetry of the differential conductance curves between $t_f/t_c = -0.066$ and $+0.01$. The origin of this enhancement/suppression can be understood from the weak tunneling limit of the current, Eq.(5.7), as it lies in the interference term $\sim t_c t_f$. For $t_f < 0$, this interference term leads to a backflow of current from the system into the tip, reducing the overall magnitude of the current, as shown in Fig. 5.3(a) where we present the contributions arising from the three terms proportional to t_c^2, t_f^2 and $2t_c t_f$ in Eq.(5.7). In contrast, for $t_f > 0$, the interference term leads to an additional current flowing from the tip into the system as shown in Fig. 5.3(b), thus increasing the total current.

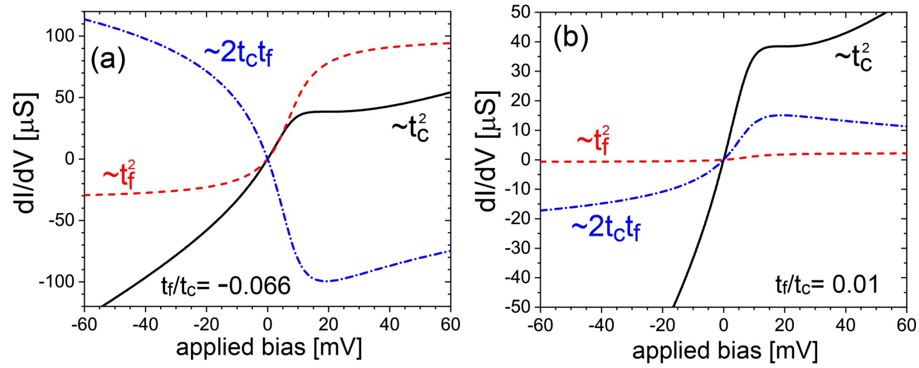

Figure 5.3: The three contributions to the total current from the weak-tunneling limit of Eq.(5.7) which are proportional to t_c^2, t_f^2 and $2t_c t_f$ for (a) $t_f/t_c = -0.066$, and (b) $t_f/t_c = +0.01$.

It also follows from the IV-curves that the magnitude of the current for bias of a few mV falls within the experimentally accessible range, implying that the value of $t_c = 0.1$eV is experimentally achievable.

In Fig.5.2(c) we present the zero-frequency shot-noise, S_0, for the cases $t_f/t_c = -0.066, +0.01$ and $r = \infty$. Similar to the current, we find that the Kondo correlations either suppress (for $t_f/t_c = -0.066$) or enhance (for $t_f/t_c + 0.01$) the shot-noise with respect to its form at $r = \infty$. The reason for suppression/enhacement is similar to that for the current: due to the backflow of the current from the system into the tip arising from the interference term for $t_f/t_c < 0$, the contribution to the noise arising from the current-current correlation between the current flowing directly from the tip into the system, and the backflow is negative, thus reducing the overall noise. In contrast, for $t_f/t_c > 0$ the contribution to the noise $\sim t_c t_f$ is positive, leading to an enhanced noise in the vicinity of the Kondo resonance. Finally, in Fig.5.2(d) we present the Fano factor for all three cases, which exhibits a peak near the Kondo resonance for $t_f/t_c = -0.066$, and a dip for $t_f/t_c = 0.01$. Moreover, the Fano factor for $t_f/t_c = -0.066$ near the Kondo resonance is enhanced over its value for $r = \infty$, while it is suppressed for $t_f/t_c = 0.01$. To understand this difference in the Fano factor near $V = 0$, we consider the Landauer formula [116] for the current

$$I = \frac{e^2}{\pi\hbar} V T_{eff} \tag{5.14}$$

where T_{eff} is the effective transmission coefficient between the tip and the system. A comparison with the weak-tunneling expression for the current, Eq.(5.7), shows that to leading order in V

$$\begin{aligned} T_{eff} &= -2\pi N_t \left[t_c^2 \mathrm{Im} g_{cc}^r(\varepsilon_F) + 2 t_c t_f \mathrm{Im} g_{cf}^r(\varepsilon_F) \; + t_f^2 \mathrm{Im} g_{ff}^r(\varepsilon_F) \right] \\ &= \frac{\pi\hbar}{e^2} \left. \frac{dI}{dV} \right|_{V=0} \end{aligned} \tag{5.15}$$

It follows from Fig. 5.2(a) that $T_{eff} \sim \left. \frac{dI}{dV} \right|_{V=0}$ is smaller for $t_f/t_c = -0.066$ than for $t_f/t_c = 0.01$. Similarly, the shot-noise can be written in terms of T_{eff} as [117]

$$S = \frac{2e^3}{\pi\hbar} |V| T_{eff} (1 - T_{eff}) \; . \tag{5.16}$$

A comparison of Eq.(5.16) with the weak tunneling limit for S_0 in Eq.(5.9) yields the same T_{eff} as in Eq.(5.15) to leading order in t_c, t_f. We note that the term $\sim T_{eff}^2$ in Eq.(5.16) scales as the hopping amplitudes to the fourth power, and is therefore not contained in the weak-tunneling limit of S_0 in Eq(5.9). By combining Eqs.(5.14) and (5.16), we obtain for the Fano factor near $V = 0$ $F = (1 - T_{eff})$, which is thus larger for $t_f/t_c = -0.066$ than for $t_f/t_c = 0.01$, in agreement with our numerical results shown in Fig.5.2(d). We thus conclude that there exist an interesting correlation between the lineshape of the Kondo resonance (as determined by t_f/t_c) and the enhancement or suppression of the Fano factor with respect to the $r = \infty$ result.

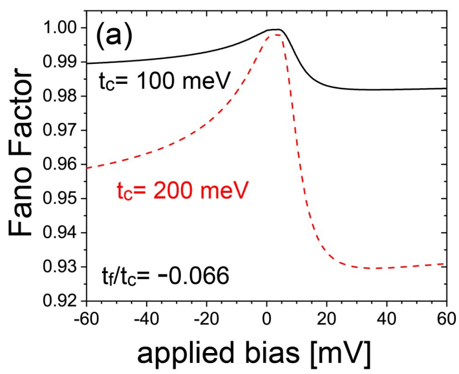

Figure 5.4: Evolution of the Fano factor F with increasing t_c for (a) $t_f/t_c = -0.066$, and (b) $t_f/t_c = 0.01$

A unique feature of the Fano factor is that its overall lineshape, i.e, its bias dependence, is essentially independent of t_c, varying only with t_f/t_c. To demonstrate this, we present in Fig. 5.4 F for several values of t_c with constant t_f/t_c. While the overall lineshape of the Fano factor does not change with increasing t_c (for constant t_f/t_c), its overall variation increases, thus becoming easier to observe experimentally. It is interesting to note that the maximum of the Fano factor for $t_f/t_c = -0.066$ remains close to unity in the Kondo resonance, implying that the transmission amplitude T_{eff} remains approximately zero. On the other hand, for $t_f/t_c = +0.01$, the suppression of the Fano factor near the Kondo resonance increases, implying that T_{eff} increases with increasing t_c.

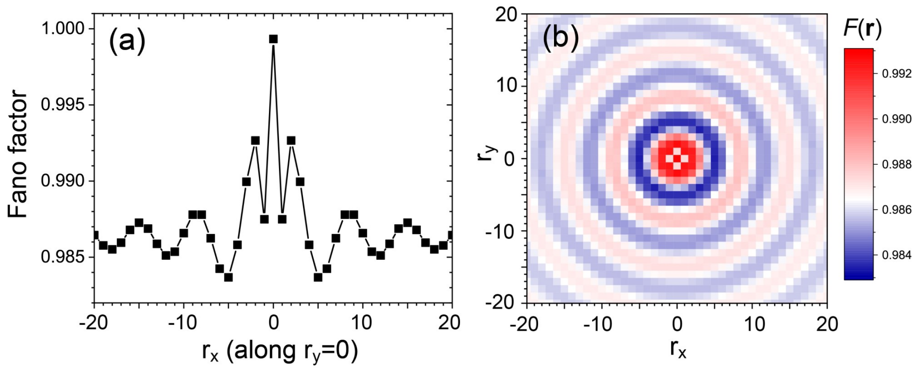

Figure 5.5: (a) Linecut of F through the site the magnetic adatom for $t_c = 0.1$ eV, $V = 5$mV and $t_f/t_c = -0.066$. (b) Spatial plot of F.

The Fano factor exhibits spatial oscillations, as shown in Fig. 5.5, where we present a linecut of the Fano factor through the magnetic adatom [Fig. 5.5(a)] as well as a spatial plot of $F(\mathbf{r})$

[Fig. 5.5(b)]. The spatial plot of $F(\mathbf{r})$ reveals nearly isotropic oscillations whose wavelength is given by $\lambda \approx 6.5a_0$ which is half of the Fermi wave-length. We can therefore conclude that the spatial oscillations of the Fano factor are $2k_F r$-oscillations, arising from scattering of the surface conduction electrons from the magnetic adatom. Similar spatial oscillations in the conductance fluctuations were interpreted as a signature of the Kondo screening cloud [89].

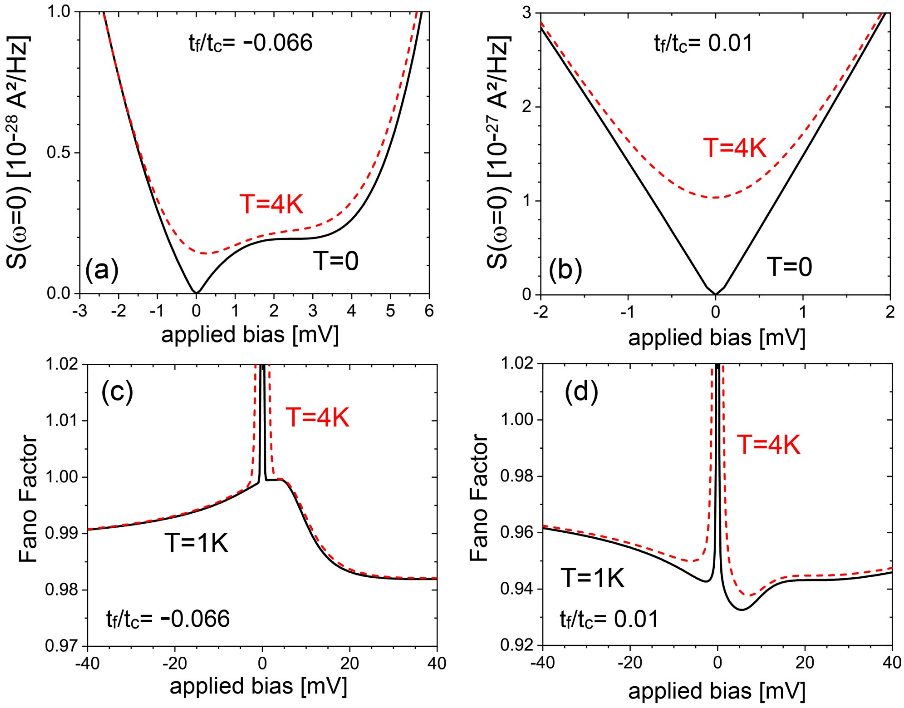

Figure 5.6: Comparison of the zero-frequency noise, $S(\omega = 0)$, at $T = 0$ and $T = 4K$ for $t_c = 0.1$eV and (a) $t_f/tc = -0.066$, and (b) $t_f/tc = 0.01$ (note the different x- and y-axes scales). Temperature evolution of the Fano factor for $t_c = 0.1$eV and (c) $t_f/tc = -0.066$, and (d) $t_f/tc = 0.01$.

Finally, we briefly comment on the temperature dependence of the Fano factor. For any non-zero temperature, there are thermal contributions to the zero-frequency noise which are non-zero even at $V = 0$, as shown in Figs. 5.6(a) and (b) for $t_f/tc = -0.066$ and 0.01, respectively (note the different x- and y-axes scales). On the other hand, the current vanishes for $V = 0$, independent of temperature. This implies that for any non-zero temperature, the Fano factor exhibits a divergence at $V = 0$, as shown in Fig. 5.6(c) and (d). We note that the bias range over which the Fano factor at $T = 4K$ is enhanced over its $T = 0$ value is significantly larger for $t_f/t_c = 0.01$.

5.3 Shot noise in a Kondo lattice

We next study the form of the current and shot-noise in a Kondo lattice. To this end, we consider two different sets of parameters for the Kondo lattice model of Eq.(5.10) previously considered in Ref. [43]: one in which the antiferromagnetic interaction is sufficiently small [$I/J = 0.001$, Kondo lattice 1 (KL1)], such that the system exhibits a hard hybridization gap [see Figs. 5.7(a) and 5.8(a)], and one in which the antiferromagnetic interaction is so strong enough [$I/J = 0.015$, Kondo lattice 2 (KL2)] such that the system's dispersion does not any longer exhibit an indirect gap [see Fig. 5.7(b)] and the hybridization gap is seen as a suppression in dI/dV rather than hard gap (see Fig. 5.10(a), for a more in-depth review, see Ref. [44]).

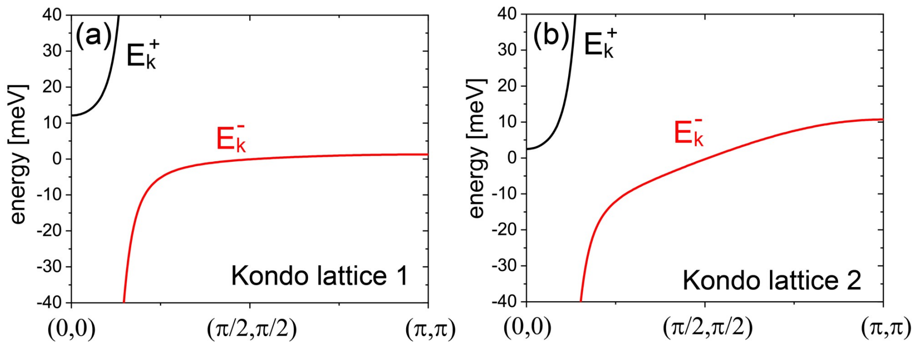

Figure 5.7: The dispersions $E_{\mathbf{k}}^{\pm}$ from Eq.(5.13) along $(0,0) \to (\pi,\pi)$ with $t = 500meV$, $\mu = -3.618t$, $N = 2$, $J = 500$meV, $N_t = 1eV^{-1}$, for (a) Kondo lattice 1 with $I/J = 0.001$ yielding $s = 48.5$meV, $\varepsilon_f = 1.2$meV, and $\chi_0 = 0.17$meV, and (b) Kondo lattice 2 with $I/J = 0.015$ yielding $s = 48.0$meV, $\varepsilon_f = 0.94$meV, and $\chi_0 = 2.59$meV.

We begin by considering the form of the noise and Fano factor for Kondo lattice 1 and present in Fig. 5.8(a) the differential conductance for two different values of $t_f/t_c = \pm 0.015$. As expected, dI/dV exhibits a hard hybridization gap, and very different asymmetries for the two values of t_f/t_c, similar to the case of a single Kondo impurity shown in Fig. 5.2.

In Figs. 5.8(b) and (c), we present the resulting current and shot-noise. Both the current and the shot-noise are essentially bias independent inside the hybridization gap, but overall show a very similar bias dependence to that of the single Kondo impurity. Finally, in Fig. 5.8(d) we show the resulting Fano factor. Similar to the single Kondo impurity, the Fano factor is correlated with the asymmetry of the differential conductance. For $t_f/t_c = -0.015$, the Fano factor is close to unity in the hybridization gap, implying that the transmission coefficient is small. In contrast, for $t_f/t_c = +0.015$, the Fano factor is strongly suppressed near the hybridization gap, implying a much larger transmission coefficient. Comparing the Fano factor with that of an

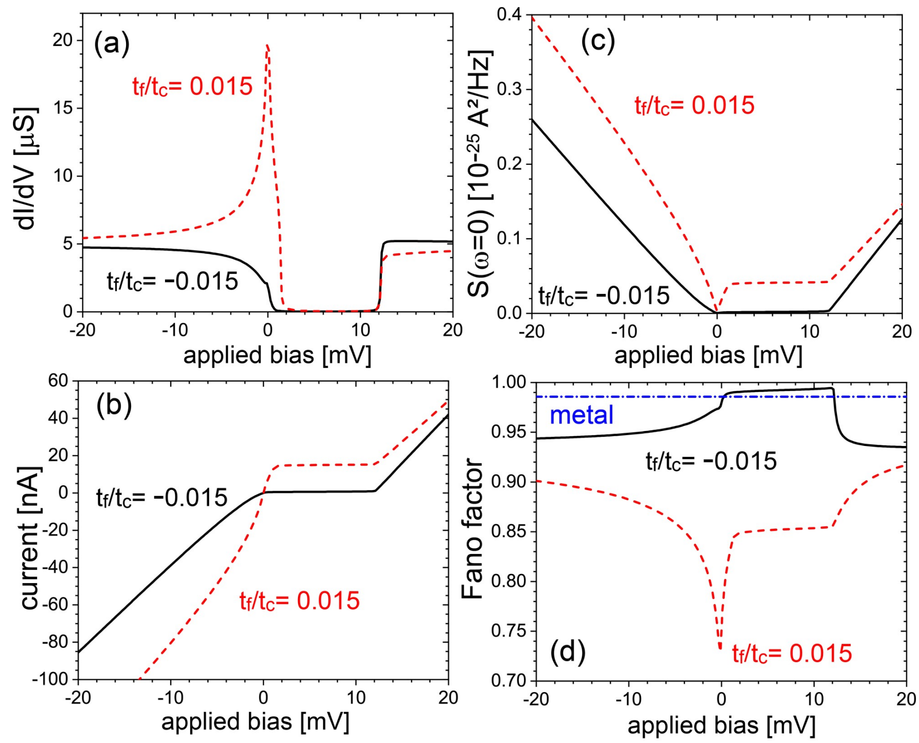

Figure 5.8: For Kondo lattice 1: (a) dI/dV, (b) current, (c) noise, and (d) Fano factor with $t_c = 0.1$ eV and two different values of t_f/t_c.

uncorrelated metal shows that the strong correlations arising from Kondo screening lead to an overall suppression of the Fano factor independent of the value of t_f/t_c, except for the immediate vicinity of the hybridization gap for $t_f/t_c = -0.015$, where the Fano factor is slightly larger than that of the metallic systems.

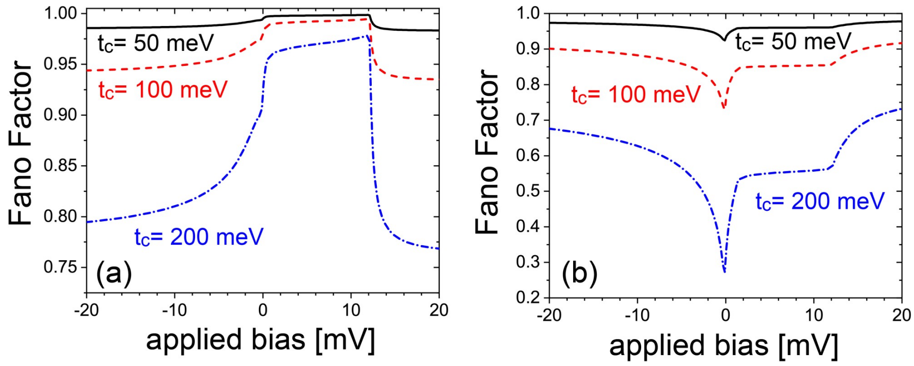

Figure 5.9: Evolution of the Fano factor F with increasing t_c in Kondo lattice 1 for (a) $t_f/t_c = -0.015$, and (b) $t_f/t_c = 0.015$.

Similar to the case of the single impurity, we find that the overall shape of the Fano factor is independent of the tunneling amplitudes t_c, t_f (for fixed t_f/t_c), as shown in Fig. 5.9, and that only the overall variation of the Fano factor increases with increasing tunneling amplitudes.

We next consider the form of the noise and Fano factor in Kondo lattice 2, and present in

Fig. 5.10(a) the resulting differential conductance for two different values of $t_f/t_c = -0.03, 0.01$. The larger antiferromagnetic interaction (in comparison to KL1), and the resulting larger value of χ_0, give rise to two interesting effects: (a) dI/dV does not any longer show a hard hybridization gap, but only a suppression, and (b) the van-Hove singularity of the heavy f-electron band has been moved inside the hybridization gap, as particularly evident for $t_f/t_c = 0.01$. Both features are qualitatively similar to the ones found in the differential conductance of the heavy fermion material URu_2Si_2 [118, 119].

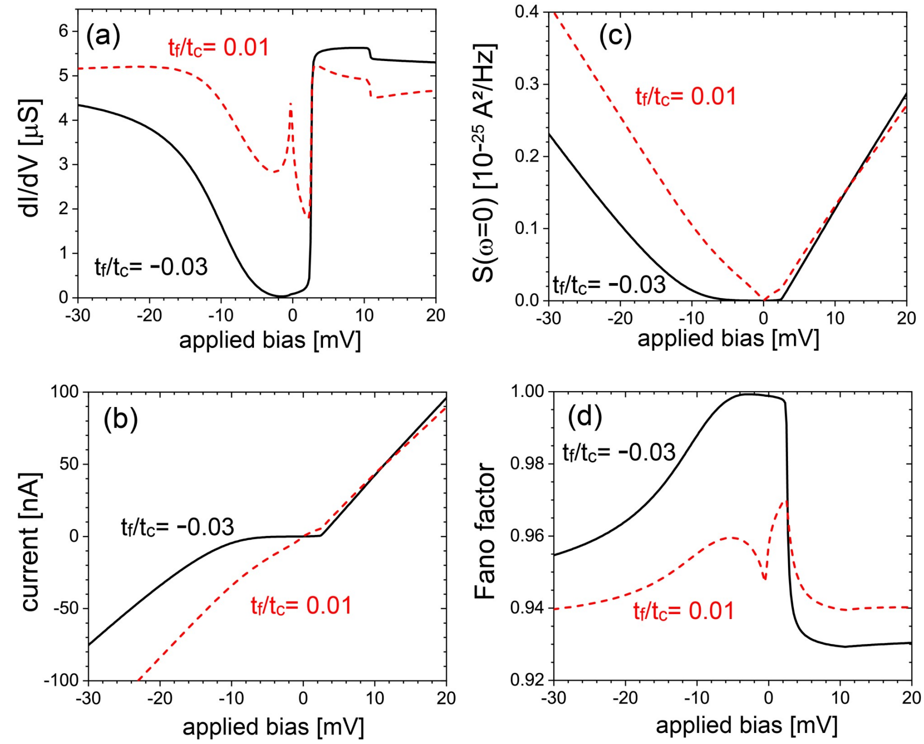

Figure 5.10: For Kondo lattice 2: (a) dI/dV, (b) current, (c) noise, and (d) Fano factor with $t_c = 0.1$ eV and two different values of t_f/t_c.

Similar to the dI/dV, the current and shot-noise shown in Figs. 5.10(b) and (c) differ significantly for negative bias $V < 0$, while being quite similar for positive bias $V > 0$. In Fig. 5.10(d) we present the resulting Fano factor. For $t_f/t_c = -0.03$ where the suppression of dI/dV is the more pronounced, the Fano factor is close to unity, implying a vanishing T_{eff}. Interestingly enough, the van-Hove singularity inside the hybridization gap leads to a strong suppression of the Fano factor at the same bias for $t_f/t_c = 0.01$. This strong correlation between the form of the differential conductance and the Fano Factor represents an important test for future STSNS experiments.

Conclusions

This work has investigated magnetic-superconductor hybrid (MSH) systems in order to discern their topological properties and understand the possibilities for engineering various Majorana states. We began by reporting the engineering of topological superconductivity and direct visualization of theoretically predicted Majorana edge modes in a nano-scale Fe island located on a Re(0001)-O(2×1) substrate. The combination of spatially resolved spectroscopy and topography allowed the Wiesendanger group to not only to correlate for the first time the energy and spatial dependence of the observed in-gap edge modes with the physical edge of the Fe island, but also to demonstrate the robustness of these edge modes against edge disorder. Both of these experimental observations, which are in very good agreement with our theoretical calculations, represent hallmarks of the modes' topological nature. Our theoretical studies demonstrate that the emergence of topological superconductivity in Fe/Re(0001)-O(2×1) does not require any fine-tuning of parameters, but is expected over a wide range of band parameters and magnetic structures. Moreover, we demonstrated that the emergence of topological superconductivity in such a hybrid magnet-superconductor system is only made possible through interface engineering using an atomically thin separation layer.

Additionally, we have demonstrated that it is possible to use atomic manipulation techniques to adiabatically tune MSH structures between 1D and 2D topological superconducting phases. Specifically, we showed that while two-dimensional chiral topological superconductors (with $\mathbb{Z}$ classification) and one-dimensional topological superconductors (with $\mathbb{Z}_2$ classification) are in different universality classes, the system does not undergo a phase transition if one transforms a 2D Shiba island via a hybrid chain-island structure into a 1D chain by adding or removing adatoms. Moreover, by attaching Shiba chain networks to Shiba islands, we showed that one can arbitrarily transform chiral Majorana edge modes into localized Majorana bound states, and vice versa. This, in turn, opens a new real space approach to counting the Chern number of topological superconductors. In particular, when a Shiba island is in a topological phase with Chern number C, then the spectral weight of the zero-energy chiral Majorana edge modes completely vanishes when $2|C|$ chains are attached to it, as the Majorana modes are transformed into Majorana bound states localized at the end of the chains. We have explicitly demonstrated these results for a series of Chern numbers ($C = 1, 2, 3, 4$) and for different lattice geometries, as well as in the experimentally relevant MSH model that was successfully employed to explain the emergence of chiral Majorana edge modes in Fe/Re-O(2×1). Finally, we demonstrated that the topological nature of MSH structures can the characterized through the Chern number density, which adiabatically connects between finite-size MSH structures and translationally invariant, macroscopic systems that are characterized by an integer Chern number. The direct real space visualization of Majorana edge modes demonstrated in Ch. 2, in combination with STM-based single-atom manipulation techniques [18,48], opens unprecedented opportunities to realize topological phases in artificial 2D magnetic adatom arrays on elemental superconducting substrates providing fascinating building blocks for future topological quantum computer architectures.

Further, we proposed and developed a model of $FeSe_{0.45}Te_{0.55}$ that combined Rashba spin-orbit coupling and surface magnetism with a previously formulated 5-band model based on results of STS experiments. Using our extended model, we calculated the phase diagram of $FeSe_{0.45}Te_{0.55}$ over a range of global chemical potentials and exchange couplings and found Chern numbers ranging from -3 to 1. Our model poses an alternative explanation of the emergence of topological superconductivity in $FeSe_{0.45}Te_{0.55}$, in contrast to prior explanations that rely on the bulk material being a topological insulator. In addition, we calculated the local density of states across a vortex in a generic $s_{\pm}$ superconductor model and find that parameter sets both in and out of a topological phase exhibit regularly spaced trivial Caroli-de Gennes-Matricon states. By contrast, only the topological phase exhibits a state at zero energy in the vortex core, indicating a MBS. This MBS is strongly spin-polarized giving experimentalists a powerful benchmark for verifying the existence of MBSs in real systems.

Finally, we have investigated the relation between the differential conductance, current, noise and the resulting Fano factor measured via shot noise scanning tunneling spectroscopy around a single Kondo impurity as well as in a Kondo lattice. We demonstrated that the lineshape of the Fano factor, i.e., its bias dependence, represents a characteristic variation arising from Kondo screening, similar to the Kondo resonance observed in the differential conductance. Moreover, the lineshape of F is strongly dependent on the ratio of the tunneling amplitudes t_f/t_c and can be enhanced or suppressed due to interference effects arising from tunneling into the conduction and f-electron levels. As such, it is not only a sensitive probe for the correlation effects arising from Kondo screening, but also for quantum interference between tunneling electrons. Moreover, we showed that near the Fermi energy, there exists a correlation between the form of dI/dV and F through the effective transmission coefficient T_{eff}, such that a suppression in dI/dV leads to a value of F near unity, while a peak in dI/dV gives rise to a strong suppression in F. We also predicted that around a single Kondo impurity, the Fano factor exhibits spatial oscillations whose wavelength arises from $2k_F r$ oscillations of the scattered conduction electrons. In Kondo lattices, we find that the Fano factor possesses a correlation with the differential conductance that is similar to that in the single Kondo impurity case. This correlation represents a prediction of the effects of quantum interference arising from multiple tunneling paths that could be tested in future STSNS experiments.

Appendix A

Copyright Permissions

Per American Physical Society (https://journals.aps.org/copyrightFAQ.html#thesis)

> As the author of an APS-published article, may I include my article or a portion of my article in my thesis or dissertation?
>
> Yes, the author has the right to use the article or a portion of the article in a thesis or dissertation without requesting permission from APS, provided the bibliographic citation and the APS copyright credit line are given on the appropriate pages.

This applies to

"Dimensional tuning of Majorana fermions and real space counting of the Chern number"

Eric Mascot, Sagen Cocklin, Stephan Rachel, and Dirk K. Morr

Phys. Rev. B 100, 184510 ©2019 American Physical Society

and

"Scanning tunneling shot-noise spectroscopy in Kondo systems"

Sagen Cocklin and Dirk K. Morr

Phys. Rev. B **100**, 125146 ©2019 American Physical Society

Per Science Advances

(https://www.sciencemag.org/site/feature/contribinfo/prep/4__2014LicensetoPublish_Final_6MAR2014.pdf):

"3. Author also retains the non-exclusive right to use the Work in the following ways without further permission but only after publication of the Work by AAAS and subject to the requirement that credit be given to its first publication in the appropriate issue of the applicable

Science journal: [...] 2) Reprint the Work in print format for inclusion in a thesis or dissertation that the Author writes"

This applies to

"Atomic-scale interface engineering of Majorana edge modes in a 2D magnet-superconductor hybrid system"

Science Advances 26 Jul 2019:

Alexandra Palacio-Morales, Eric Mascot, Sagen Cocklin, Howon Kim, Stephan Rachel, Dirk K. Morr, and Roland Wiesendanger

Vol. 5, no. 7, eaav6600

Copyright © 2019 The Authors, some rights reserved; exclusive licensee American Association for the Advancement of Science. No claim to original U.S. Government Works. Distributed under a Creative Commons Attribution NonCommercial License 4.0 (CC BY-NC).

Bibliography

[1] K. Von Klitzing, G. Dorda, M. Pepper. New method for high-accuracy determination of the fine-structure constant based on quantized Hall resistance. *Physical Review Letters* **45**, 494 (1980).

[2] D. J. Thouless, M. Kohmoto, M. P. Nightingale, M. Den Nijs. Quantized Hall Conductance in a Two-Dimensional Periodic Potential. *Physical Review Letters* **49**, 405 (1982).

[3] E. Majorana. Teoria simmetrica dell'elettrone e del positrone. *Nuovo Cimento* **14**, 171 (1937)

[4] G. Moore and N. Read. Nonabelions in the fractional quantum hall effect. *Nuclear Physics B* **360**, 362 (1991).

[5] C. Nayak, S. H. Simon, A. Stern, M. Freedman, S. Das Sarma. Non-Abelian anyons and topological quantum computation. *Review of Modern Physics* **80**, 1083 (2008).

[6] C. W. J. Beenakker. Developments in Topological Insulators. *Annual Review Condensed Matter Physics* **4**, 113–136 (2011).

[7] J. Alicea. New directions in the pursuit of Majorana fermions in solid state systems. *Reports on Progress in Physics* **75**, 076501 (2012).

[8] F. Wilczek. Majorana Returns. *Nature Physics* **5**, 614–618 (2009).

[9] D. A. Ivanov. Non-Abelian Statistics of Half-Quantum Vortices in p-Wave Superconductors. *Physical Review Letters* **86**, 268–271 (2001).

[10] S. R. Elliott, M. Franz. Colloquium: Majorana fermions in nuclear, particle, and solid-state physics. *Review of Modern Physics* **87**, 137–163 (2015).

[11] M. Sato, Y. Ando. Topological superconductors: a review. *Reports on Progress in Physics* **80**, 076501 (2017).

[12] A. Y. Kitaev. Unpaired Majorana fermions in quantum wires. *Physics-Uspekhi* **44**, 131 (2001).

[13] E. F. Talantsev, K. Iida, T. Ohmura, T. Matsumoto, W. P. Crump, N. M. Strickland, S. C. Wimbush, H. Ikuta. p-wave superconductivity in iron-based superconductors. *Scientific Reports* **9**, 14245 (2019).

[14] V. Mourik, K. Zuo, S. M. Frolov, S. R. Plissard, E. P. A. M. Bakkers, and L. P. Kouwenhoven. Signatures of Majorana fermions in hybrid superconductor-semiconductor nanowire devices. *Science* **336**, 1003 (2012).

[15] R. M. Lutchyn, J. D. Sau, S. Das Sarma. Majorana fermions and a topological phase transition in semiconductor-superconductor heterostructures. *Physical Review Letters* **105**, 077001 (2010).

[16] Y. Oreg, G. Refael, F. von Oppen. Helical liquids and Majorana bound states in quantum wires. *Physical Review Letters* **105**, 177002 (2010).

[17] S. Nadj-Perge, I. K. Drozdov, J. Li, H. Chen, S. Jeon, J. Seo, A. H. MacDonald, B. A. Bernevig, and A. Yazdan. Observation of Majorana fermions in ferromagnetic atomic chains on a superconductor. *Science* **346**, 602 (2014).

[18] H. Kim, A. Palacio-Morales, T. Posske, L. Rozsa, K. Palotas, L. Szunyogh, M. Thorwart and R. Wiesendanger. Toward tailoring Majorana bound states in artificially constructed magnetic atom chains on elemental superconductors. *Science Advances* **4**, eaar5251 (2018).

[19] M. Ruby, F. Pientka, Y. Peng, F. von Oppen, B. W. Heinrich, and K. J. Franke. End states and subgap structure in proximity-coupled chains of magnetic adatoms. *Physical Review Letters* **115**, 197204 (2015).

[20] R. Pawlak, M. Kisiel, J. Klinovaja, T. Meier, S. Kawai, T. Glatzel, D. Loss and E. Meyer.Probing atomic structure and Majorana wavefunctions in mono-atomic Fe chains on superconducting Pb surface. *npj Quantum Information* **2**, 16035 (2016).

[21] J. Li, T. Neupert, Z. Wang, A. H. MacDonald, A. Yazdani, B. Andrei Bernevig.Two-dimensional chiral topological superconductivity in Shiba lattices. *Nature Communications* **7**, 12297 (2016).

[22] J. Röntynen, T. Ojanen. Topological superconductivity and high Chern numbers in 2D ferromagnetic Shiba lattices. *Physical Review Letters* **114**, 236803 (2015).

[23] S. Rachel, E. Mascot, S. Cocklin, M. Vojta, D. K. Morr. Quantized charge transport in chiral Majorana edge modes. *Physical Review B* **96**, 205131 (2017).

[24] K. Björnson, A. M. Black-Schaffer. Probing chiral edge states in topological superconductors through spin-polarized local density of state measurements. *Physical Review B* **97**, 140504 (2018).

[25] G. C. Menard, S. Guissart, C. Brun, R. T. Leriche, M. Trif, F. Debontridder, D. Demaille, D. Roditchev, P. Simon and T. Cren. Two-dimensional topological superconductivity in Pb/Co/Si (111). *Nature Communication* **8**, 2040 (2017).

[26] A. Palacio-Morales, E. Mascot, S. Cocklin, H. Kim, S. Rachel, D. K. Morr, and R. Wiesendanger. Atomic-Scale Interface Engineering of Majorana Edge Modes in a 2D Magnet-Superconductor Hybrid System. *Science Advances* eaav6600 (2019).

[27] G. C. Ménard, A. Mesaros, C. Brun, F. Debontridder, D. Roditchev, P. Simon, and T. Cren. Isolated pairs of Majorana zero modes in a disordered superconducting lead monolayer. *Nature Communications* **10**, 2587 (2019)

[28] P. Zhang, K. Yaji, T. Hashimoto, Y. Ota, T. Kondo, K. Okazaki, Z. Wang, J. Wen, G. D. Gu, H. Ding, S. Shin. Observation of topological superconductivity on the surface of an iron-based superconductor. *Science* **360**, 182 (2018)

[29] D. Wang, L. Kong, P. Fan, H. Chen, S. Zhu, W. Liu, L. Cao, Y. Sun, S. Du, J. Schneeloch, R. Zhong, G. Gu, L. Fu, H. Ding, and H.-J. Gao. Evidence for Majorana bound states in an iron-based superconductor. *Science* **362**,333 (2018)

[30] T. Machida, Y. Sun, S. Pyon, S. Takeda, Y. Kohsaka, T. Hanaguri, T. Sasagawa, and T. Tamegai. Zero-energy vortex bound state in the superconducting topological surface state of Fe (Se, Te). *Nature Materials* **18**, 811 (2019)

[31] C. Chen, K. Jiang, Y. Zhang, C. Liu, Y. Liu, Z. Wang, J. Wang. Atomic line defects and zero-energy end states in monolayer Fe (Te, Se) high-temperature superconductors. *Nature Physics* **16**, 536 (2020)

[32] Z. Wang, J. O. Rodriguez, L. Jiao, S. Howard, M. Graham, G. D. Gu, T. L. Hughes, D. K. Morr, and V. Madhavan. Evidence for dispersing 1D Majorana channels in an iron-based superconductor. *Science* **367**, 104 (2020).

[33] C-K Chiu, J. C. Y. Teo, A. P. Schnyder, and S. Ryu. Classification of topological quantum matter with symmetries. *Review of Modern Phyics.* **88**, 035005 (2016)

[34] A. A. Abrikosov. On the magnetic properties of superconductors of the second group. *Soviet Journal of Experiemental and Theoretical Physics* **5**, 1174 (1957); *Phys. Chem. Solids* **2**, 199 (1957).

[35] Laura Fanfarillo, Joseph Mansart, Pierre Toulemonde, Hervé Cercellier, Patrick Le Fèvre, François Bertran, Belen Valenzuela, Lara Benfatto, and Véronique Brouet. Orbital-dependent Fermi surface shrinking as a fingerprint of nematicity in FeSe. *Physical Review B* **94**, 155138 (2016)

[36] J. Kondo. Resistance minimum in dilute magnetic alloys. *Progress of Theoretical Physics* **32**, 37 (1964).

[37] V. Madhavan, W. Chen, T. Jamneala, M. F. Crommie, N. S. Wingreen. Tunneling into a single magnetic atom: spectroscopic evidence of the Kondo resonance. *Science* **280**, 567 (1998).

[38] J. Li, W.-D. Schneider, R. Berndt, and B. Delle. Kondo scattering observed at a single magnetic impurity. *Physical Review Letters* **80**, 2893 (1998).

[39] H.C. Manoharan, C.P. Lutz, and D.M. Eigler. Quantum mirages formed by coherent projection of electronic structure. *Nature* (London) **403**, 512 (2000).

[40] V. Madhavan, W. Chen, T. Jamneala, M. F. Crommie, and N. S. Wingreen. Local spectroscopy of a Kondo impurity: Co on Au(111). *Physical Review B* **64**, 165412 (2001).

[41] N. Knorr, M. A. Schneider, L. Diekhöner, P. Wahl, and K. Kern. Kondo Effect of Single Co Adatoms on Cu Surfaces. *Physical Review Letters* **88**,096804 (2002).

[42] U. Fano. Effects of configuration interaction on intensities and phase shifts. *Physical Review* **124**, 1866 (1961).

[43] J. Figgins and D.K. Morr. Differential conductance and quantum interference in Kondo systems. *Physical Review Letters* **104**, 187202 (2010).

[44] D.K. Morr. Theory of scanning tunneling spectroscopy: from Kondo impurities to heavy fermion materials. *Reports on Progress in Physics.* **80**, 014502 (2016).

[45] M. Maltseva, M. Dzero, and P. Coleman. Electron cotunneling into a Kondo lattice. *Physical Review Letters* **103**, 206402 (2009).

[46] A. P. Schnyder, S. Ryu, A. Furusaki, A. W. W. Ludwig. Classification of topological insulators and superconductors in three spatial dimensions. *Physical Review B* **78**, 195125 (2008).

[47] A. Kitaev. Periodic table for topological insulators and superconductors. *AIP Conference Proceedings* **22**, 1134 (2009).

[48] D. M. Eigler, E. K. Schweizer. Positioning single atoms with a scanning tunnelling microscope. *Nature.* **344**, 524–526 (1990).

[49] P. Kaghazchi, T. Jacob. Structure of rhenium surfaces in an oxygen environment. *Physical Review B* **83**, 035417 (2011).

[50] L. Yu. Bound state in superconductors with paramagnetic impurities. *Acta Physica Sinica.* **21** (1965), pp. 75–91.

[51] H. Shiba. Classical spins in superconductors. *Progress of Theoretical Physics* **40**, 435–451 (1968).

[52] A. I. Rusinov. Theory of gapless superconductivity in alloys containing paramagnetic impurities. *Soviet Journal of Experiemental and Theoretical Physics* **29**, 1101 (1969).

[53] A. V. Balatsky, I. Vekhter, J.-X. Zhu. Impurity-induced states in conventional and unconventional superconductors. *Review of Modern Physics* **78**, 373–433 (2006).

[54] L. Cornils, A. Kamlapure, L. Zhou, S. Pradhan, A. A. Khajetoorians, J. Fransson, J. Wiebe, and R. Wiesendanger. Spin-Resolved Spectroscopy of the Yu-Shiba-Rusinov States of Individual Atoms. *Physical Review Letters* **119**, 197002 (2017).

[55] X.-L. Qi, S.-C. Zhang. Topological insulators and superconductors. *Review of Modern Physics* **83**, 1057–1110 (2011).

[56] M. Bode, A. Kubetzka, K. von Bergmann, O. Pietzsch, R. Wiesendanger. Spin-polarized scanning tunneling microscopy: Insight into magnetism from nanostructures to atomic scale spin structures. *Microscopy Research and Technique* **66**, 117–125 (2005).

[57] A. Palacio-Morales, A. Kubetzka, K. von Bergmann, R. Wiesendanger. Coupling of coexisting noncollinear spin states in the Fe monolayer on Re (0001). *Nano Letters* **16**, 6252–6256 (2016).

[58] G. E. Volovik. An analog of the quantum Hall effect in a superfluid 3He film. Sov. Phys. JETP. **67**, 1804 (1988).

[59] S. Ouazi, T. Pohlmann, A. Kubetzka, K. von Bergmann, R. Wiesendanger. Scanning tunneling microscopy study of Fe, Co and Cr growth on Re (0001). *Surface Science* **630**, 280–285 (2014).

[60] R. Pantel, M. Bujor, J. Bardolle. Oxygen adsorption on various vicinal faces close to the (0001) basal plane of rhenium. *Surface Science* **83**, 228–242 (1979).

[61] R. C. Dynes, V. Narayanamurti, J. P. Garno. Direct measurement of quasiparticle-lifetime broadening in a strong-coupled superconductor. *Physical Review Letters* **41**, 1509–1512 (1978).

[62] D. Choi, Ca. Rubio-Verdú, J. de Bruijckere, M. M. Ugeda, N. Lorente, J. Ignacio Pascual. Mapping the orbital structure of impurity bound states in a superconductor. *Nature Communications* **8**, 15175 (2017).

[63] D. L. Phillips. A technique for the numerical solution of certain integral equations of the first kind. *Journal of the ACM.* **9**, 84–97 (1962).

[64] S. Twomey. On the numerical solution of Fredholm integral equations of the first kind by the inversion of the linear system produced by quadrature. *Journal of the ACM.* **10**, 97–101 (1963).

[65] M. Ternes, W.-D. Schneider, J.-C. Cuevas, C. P. Lutz, C. F. Hirjibehedin, and A. J. Heinrich. Subgap structure in asymmetric superconducting tunnel junctions. *Physical Review B* **74**, 132501 (2006).

[66] J. C. Slater, G. F. Koster. Simplified LCAO method for the periodic potential problem. *Physical Review* **94**, 1498–1524 (1954).

[67] D. A. Papaconstantopoulos, Handbook of the Band Structure of Elemental Solids: from Z=1 to Z=112 (Springer US, Boston, MA, 2015; http://link.springer.com/10.1007/978-1-4419-8264-3).

[68] M. Tinkham, Introduction to Superconductivity: Second Edition (Dover Publications, 2004)

[69] E. Prodan. Disordered topological insulators: a non-commutative geometry perspective. *Journal of Physics A: Mathematical and Theoretical* **44**, 113001 (2011).

[70] T. Hahn. Cuba—a library for multidimensional numerical integration. *Computer Physics Communications* **168**, 78–95 (2005).

[71] N. Romming, C. Hanneken, M. Menzel, J. E. Bickel, B. Wolter, K. von Bergmann, A. Kubetzka, and R Wiesendanger. Writing and Deleting Single Magnetic Skyrmions. *Science* **341**, 636 (2013).

[72] P.-J. Hsu, A. Kubetzka, A. Finco, N. Romming, K. von Bergmann, and R. Wiesendanger. Electric-field-driven switching of individual magnetic skyrmions. *Nature Nanotechnology* **12**, 123 (2017).

[73] K. Yasuda, M. Mogi, R. Yoshimi, A. Tsukazaki, K. S. Takahashi, M. Kawasaki, F. Kagawa, and Y. Tokura. Quantized chiral edge conduction on domain walls of a magnetic topological insulator. *Science* **358**, 1311 (2017).

[74] G. Ben-Shach, A. Haim, I. Appelbaum, Y. Oreg, A. Yacoby, and B. I. Halperin. Detecting Majorana modes in one-dimensional wires by charge sensing. *Physical Review B* **91**, 045403 (2015).

[75] M. Sato, Y. Takahashi and S. Fujimoto. Non-Abelian Topological Order in s-Wave Superfluids of Ultracold Fermionic Atoms. *Physical Review B* **82**, 134521 (2010).

[76] E. Prodan, in *A Computational Non-commutative Geometry Program for Disordered Topological Insulators*, vol. 23 (Springer Briefs in Mathematical Physics, 2017).

[77] E. Mascot, C. Agrahar, S. Rachel and D. K. Morr. Stability of disordered topological superconducting phases in magnet-superconductor hybrid systems. *Physical Review B* **100**, 235102

[78] R. Bianco and R. Resta. Mapping topological order in coordinate space. *Physical Review B* **84**, 241106(R) (2011).

[79] K. Bjornson and A.M Black-Schaffer. Majorana fermions at odd junctions in a wire network of ferromagnetic impurities. *Physical Review B* **94**, 100501 (2016).

[80] S. Sarkar, J. Van Dyke, P. O. Sprau, F. Massee, U. Welp, W.-K. Kwok, J. C. S. Davis, and D. K. Morr. Orbital superconductivity, defects, and pinned nematic fluctuations in the doped iron chalcogenide $\mathrm{FeSe_{0.45}Te_{0.55}}$. *Physical Review B* **96**, 060504 (2017)

[81] S. Graser, T. A. Maier, P. J. Hirschfeld and D. J. Scalapino. Near-degeneracy of several pairing channels in multiorbital models for the Fe pnictides. *New Journal of Physics* **11** 025016 (2009)

[82] T. Hashimoto, Y. Ota, H. Q. Yamamoto, Y. Suzuki, T. Shimojima, S. Watanabe, C. Chen, S. Kasahara, Y. Matsuda, T. Shibauchi, K. Okazaki, and S. Shin. Superconducting gap anisotropy sensitive to nematic domains in FeSe. *Nature Communications* **9**, 282 (2018)

[83] I. I. Mazin, D. J. Singh, M. D. Johannes, and M. H. Du. Unconventional Superconductivity with a Sign Reversal in the Order Parameter of $LaFeAsO_{1-x}F_x$ *Physical Review Letters* **101**, 057003 (2008)

[84] M. Chen, X. Chen, H. Yang, Z. Du, X. Zhu, E. Wang, and H.-H. Wen. Discrete energy levels of Caroli-de Gennes-Matricon states in quantum limit in $\mathrm{FeSe_{0.45}Te_{0.55}}$ *Nature Communications* **9** 970 (2018)

[85] A. Burtzlaff, A. Weismann, M. Brandbyge, and R. Berndt. Shot noise as a probe of spin-polarized transport through single atoms. *Physical Review Letters* **114**, 016602 (2015).

[86] K.M. Bastiaans, D. Cho, T. Benschop, I. Battisti, Y. Huang, M.S. Golden, Q. Dong, Y. Jin, J. Zaanen, and M.P. Allan. Charge trapping and super-Poissonian noise centres in a cuprate superconductor. *Nature Physics* **14**, 1183 (2018).

[87] F. Massee, Y.K. Huang, M.S. Golden, and M. Aprili. Noisy defects in the high-T_c superconductor $Bi_2Sr_2CaCu_2O_{8+x}$. *Nature Communications* **10**, 544 (2019).

[88] Z. Nussinov, M. F. Crommie, and A. V. Balatsky. Noise spectroscopy of a single spin with spin-polarized STM. *Physical Review B* **68**, 085402 (2003).

[89] K.R.Patton, H. Hafermann, S. Brener, A. I. Lichtenstein, and M. I. Katsnelson. Probing the Kondo screening cloud via tunneling-current conductance fluctuations. *Physical Review B* **80**, 212403 (2009).

[90] Y.M. Blanter, and M. Buttiker. Shot noise in mesoscopic conductors. *Physics Reports* **336**, 1 (2000).

[91] J.-X. Zhu and A. V. Balatsky. Theory of current and shot-noise spectroscopy in single-molecular quantum dots with a phonon mode. *Physical Review B***67**, 165326 (2003).

[92] Y. Meir and A. Golub. Shot noise through a quantum dot in the Kondo regime. *Physical Review Letters* **88**, 116802 (2002).

[93] B. Dong and X. L. Lei. Effect of the Kondo correlation on the thermopower in a quantum dot. *Journal of Physics: Condensed Matter* **14**, 4963 (2002).

[94] R. Lopez and D. Sanchez. Nonequilibrium Spintronic Transport through an Artificial Kondo Impurity: Conductance, Magnetoresistance, and Shot Noise. *Physical Review Letters* **90**, 116602 (2003).

[95] R. Lopez, R. Aguado, and G. Platero. Shot noise in strongly correlated double quantum dots. *Physical Review B* **69**, 235305 (2004).

[96] B.H. Wu, J.C. Cao, JC, and K.H. Ahn. Transport through a strongly correlated quantum dot with Fano interference. *Physical Review B* **72**, 165313 (2005).

[97] E. Sela, Y. Oreg, F. von Oppen, and J. Koch. Fractional shot noise in the Kondo regime. *Physical Review Letters.* **97**, 086601 (2006).

[98] O. Zarchin, M. Zaffalon, M. Heiblum, D. Mahalu, and V. Umansky. Two-electron bunching in transport through a quantum dot induced by Kondo correlations. *Physical Review B* **77**, 241303(R) (2008).

[99] C. Mora, X. Leyronas, and N. Regnault. Current Noise through a Kondo Quantum Dot in a $SU(N)$ Fermi Liquid State. *Physical Review Letters* **100**, 036604 (2008).

[100] Y. Yamauchi, K. Sekiguchi, K. Chida, T. Arakawa, S. Nakamura, K. Kobayashi, T. Ono, T. Fujii, and R. Sakano. Evolution of the Kondo effect in a quantum dot probed by shot noise. *Physical Review Letters* **106**, 176601 (2011).

[101] M. Ferrier, T. Arakawa, T. Hata, R. Fujiwara, R. Delagrange, R. Weil, R. Deblock, R. Sakano, A. Oguri and K. Kobayashi. Universality of non-equilibrium fluctuations in strongly correlated quantum liquids. *Nature Physics* **12**, 230 (2015).

[102] T. Delattre, C. Feuillet-Palma, L. G. Herrmann, P. Morfin, J.-M. Berroir, G. Fève, B. Plaçais, D. C. Glattli, M.-S. Choi, C. Mora. T. Kontos. Noisy Kondo Impurities. *Nature Physics* **5**, 208 (2009).

[103] K. Schouteden, P. Lievens, and C. Van Haesendonck. Fourier-transform scanning tunneling microscopy investigation of the energy versus wave vector dispersion of electrons at the Au (111) surface. *Physical Review B* **79**, 195409 (2009).

[104] P. Coleman. $\frac{1}{N} expansion for the Kondo lattice$ *Physical Review* **28**, 5255 (1983).

[105] A.C. Hewson, A.C. *(Cambridge University Press, Cambridge, England, 1993).*

[106] T. Senthil, M. Vojta, M. and S. Sachdev. Weak magnetism and non-Fermi liquids near heavy-fermion critical points. *Physical Review B* **69**, 035111 (2004).

[107] I. Paul, C. Pepin, and M.R. Norman. Kondo Breakdown and Hybridization Fluctuations in the Kondo-Heisenberg Lattice. *Physical Review Letters* **98**, 026402 (2007).

[108] N. Read and D.M. Newns. On the solution of the Coqblin-Schreiffer Hamiltonian by the large-N expansion technique. *Journal of Physics C: Solid State Physics* **16**, 3273 (1983).

[109] N.E. Bickers. Review of techniques in the large-N expansion for dilute magnetic alloys. *Reviews of Modern Physics* **59**, 845 (1987).

[110] I. Affleck and B. Marston. Large-n limit of the Heisenberg-Hubbard model: Implications for high-T_c superconductors. *Physical Review B* **37**, 3774 (1988).

[111] L. V. Keldysh. Diagram technique for nonequilibrium processes. *Soviet Journal of Experiemental and Theoretical Physics* **20**, 1018 (1965).

[112] J. Rammer and H. Smith. Quantum field-theoretical methods in transport theory of metals. *Reviews of Modern Physics* **58**, 323 (1986), and references therein.

[113] C. Caroli, R. Combescot, P Nozieres, and D Saint-James. Direct calculation of the tunneling current. *Journal of Physics C: Solid State Physics* **4**, 916 (1971).

[114] H. Kim, and Y. Hasegawa. Site-Dependent Evolution of Electrical Conductance from Tunneling to Atomic Point Contact. *Physical Review Letters* **114**, 206801 (2015).

[115] H. Kim, Y. Yoshida, C.-C. Lee, T.-R. Chang, H.-T. Jeng, H. Lin, Y. Haga, Z. Fisk, and Y. Hasegawa. Atomic-scale visualization of surface-assisted orbital order. *Science Advances* **3**, eaao0362 (2017).

[116] R. Landauer. Spatial Variation of Currents and Fields Due to Localized Scatterers in Metallic Conduction. *IBM Journal of Research and Development* **1**, 223 (1957).

[117] V.A. Khlus. Current and voltage fluctuations in microjunctions between normal metals and superconductors. *Zh. ED ksp. Teor. Fiz.* **93**, 2179 (1987) [*Soviet Journal of Experiemental and Theoretical Physics* **66**, 1243 (1987)].

[118] P. Aynajian, E. H. da Silva Neto, C. V. Parker, Y. Huang, A. Pasupathy, J. Mydosh, and A. Yazdani. Visualizing the formation of the Kondo lattice and the hidden order in URu2Si2. *Proceedings of the National Academy of Science, USA* **107**, 10383 (2010).

[119] T. Yuan, J. Figgins, and D.K. Morr. Hidden order transition in URu_2Si_2 Evidence for the emergence of a coherent Anderson lattice from scanning tunneling spectroscopy. Phys. Rev. B **86**, 035129 (2012).

Vita

Sagen Cocklin

Education:

Ph.D. Physics, University of Illinois at Chicago, expected August 2020.

Dissertation title: *Real-Space Properties of Topological and Correlated Systems*

B.S. Physics, Math, University of Oklahoma 2015.

Publications:

1. "Atomic-Scale Interface Engineering of Majorana Edge Modes in a 2D Magnet-Superconductor Hybrid System" A. Palacio-Morales, E. Mascot, S. Cocklin, H. Kim, S. Rachel, D. K. Morr, and R. Wiesendanger Science Advances Vol. 5, no. 7, eaav6600, 2019
2. "Dimensional tuning of Majorana fermions and real space counting of the Chern number" E. Mascot, S. Cocklin, S. Rachel, and D. K. Morr, Physical Review B 100, 184510, 2019
3. "Scanning tunneling shot-noise spectroscopy in Kondo systems" S. Cocklin and D. K. Morr Physical Review B 100, 125146, 2019.

Research Presentations:

1. Talk: "Quantum Engineering Topological Superconductors" Condensed Matter Seminar, University of Melbourne, February 2019
2. Poster:"Tuning Topological Properties of Nanoscopic Topological Superconductors Through Shape and Magnetic Structure." oSTEM 2017

Awards:

1. Fall 2018 UIC Award for Graduate Research

Schools Attended:

1. Advanced School and Workshop on Correlations in Electron Systems – from Quantum Criticality to Topology at ICTP, 2018

Teaching Experience:

Discussion Assistant	Electricity and Magnetism
Discussion Assistant	Classical Mechanics
Lab Assistant	Classical Mechanics